ADVANCED HEALTHCARE MATERIALS
www.advhealthmat.de

Drug-Eluting Porous Embolic Microspheres for Trans-Arterial Delivery of Dual Synergistic Anticancer Therapy for the Treatment of Liver Cancer

*Benzion Amoyav, Allan I. Bloom, Yoel Goldstein, Rafael Miller, Mariana Sharam, Arnon Fluksman, and Ofra Benny**

Blockage of blood supply while administering chemotherapy to tumors, using trans-arterial chemoembolization (TACE), is the most common treatment for intermediate and advanced-stage unresectable Hepatocellular carcinoma (HCC). However, HCC is characterized by a poor prognosis and high recurrence rates (≈30%), partly due to a hypoxic pro-angiogenic and pro-cancerous microenvironment. This study investigates how modifying tissue stress while improving drug exposure in target organs may maximize the therapeutic outcomes. Porous degradable polymeric microspheres (MS) are designed to obtain a gradual occlusion of the hepatic artery that nourishes the liver, while enabling efficient drug perfusion to the tumor site. The fabricated porous MS are introduced intrahepatically and designed to release a combination therapy of Doxorubicin (DOX) and Tirapazamine (TPZ), which is a hypoxia-activated prodrug. Liver cancer cell lines that are treated with the combination therapy under hypoxia reveal a synergic anti-proliferation effect. An orthotopic liver cancer model, based on N1-S1 hepatoma in rats, is used for the efficacy, biodistribution, and safety studies. Porous DOX-TPZ MS are very effective in suppressing tumor growth in rats, and induction tissue necrosis is associated with high intratumor drug concentrations. Porous particles without drugs show some advantages over nonporous particles, suggesting that morphology may affect the treatment outcomes.

1. Introduction

Tumor hypoxia is one of the key factors for the poor prognosis and efficacy of cancer therapy. This salient element plays a central role in angiogenesis, the development of drug resistance, the promotion of genomic instability, and the activation of tumor survival factors, making it a highly desirable therapeutic target.[1,2] Liver cancer is the sixth most common cancer and the third leading cause of cancer death globally, where hepatocellular carcinoma (HCC) is the most common form of liver cancer, accounting for ≈90% of cases.[3] Owing to advanced disease or underlying liver dysfunction, less than 30% of newly diagnosed HCC patients are eligible for curative treatments such as surgery, liver transplantation, or local ablation.[4] The rest of the patients receive palliative treatments including trans-arterial embolization (TAE), trans-arterial chemoembolization (TACE), chemotherapy, radioembolization, and other supportive care.[5] According to the most acceptable HCC management guidelines, the Barcelona clinic liver cancer staging system (BCLC), TACE has been recommended

B. Amoyav, Y. Goldstein, A. Fluksman, O. Benny
The Institute for Drug Research
School of Pharmacy
The Faculty of Medicine
The Hebrew University of Jerusalem
Jerusalem91120, Israel
E-mail: ofra.benny@mail.huji.ac.il

A. I. Bloom
Department of Medical Imaging-Interventional Radiology
Hadassah Medical Center
Jerusalem911200, Israel

R. Miller
Department of General Surgery
Kaplan Medical Center
Affiliated to Hebrew University Jerusalem
Rehovot 76100, Israel

M. Sharam
Authority for Biological and Biomedical Models
Hadassah Medical Center
Jerusalem 911200, Israel

The ORCID identification number(s) for the author(s) of this article can be found under https://doi.org/10.1002/adhm.202301548

DOI: 10.1002/adhm.202301548

as a promising approach for the treatment of intermediate and advanced HCC.[6] In TACE, a microcatheter locally delivers chemotherapy agents to the tumor bed, along with arterial occlusion; hence, it contributes to the localized drug uptake in tumor tissue and increases antitumor activity while reducing undesired systemic toxicity to healthy organs. Among the most common TACE methods are the conventional TACE (cTACE), which utilizes Lipiodol mixed with blocking agents (beads, gels, or others), and drug-eluting bead TACE (DEB-TACE) represented by LC Bead, Embozene, and HepaSphere. However, most of the current approaches fail to lead to satisfying clinical outcomes due to different limitations. The main drawbacks include rapid drug clearing, particles that are non-bioresorbable, polydispersity in particle physical parameters, and the lack of adaptation to the tumor microenvironment.[7]

The specific tumor niche is a critical topic to consider when designing optimal embolic agents and treatments. Several studies showed that tumor hypoxia is greatly elevated in embolic chemotherapy processes. Hypoxia constitutes a key driving force in tumor development by activating and elevating hypoxia-inducible factor 1 (HIF-1) and the expression of vascular endothelial growth factor (VEGF), suggesting that current embolism strategies might promote tumor invasion and metastasis.[8–10] Therefore, the development of biodegradable, controlled drug release carriers that can combine both cytotoxic and tumor hypoxia-inducing drugs as the embolic agents might offer a much-needed alternative therapeutic treatment to the current approaches. According to recent studies, poly(lactic-co-glycolic acid) (PLGA)-based embolic microspheres (MS) were found to be an alternative to other clinically approved TACE agents, mainly due to their excellent biocompatible and biodegradable properties.[11] Studies showed, for example, the use of PLGA for embolism to release encapsulated active agents. These experiments were performed, including MS loaded with sorafenib and contrast agent, to detect the MS post-embolization performed,[12] or fabricated PLGA MS for a synergistic combination of TACE and magnetic ablation.[13] In another study, a novel multifunctional embolic MS characterized with high drug loading capacity, local heating activity, and imaging were fabricated to ease location tracking during the embolization process.[14]

Another characteristic that must be considered during particle design and synthesis is the physical structure of the device itself. Among others, particle size, morphology, and stiffness are known to affect cell interaction, drug release, and overall physicochemical characteristics.[15,16] Polymeric MS with porous surfaces and internal structures were shown to significantly modify the drug entrapment and release patterns.[17] Noteworthy, the solubility, encapsulation efficiency, MS physical characteristics, and the release kinetics of pharmaceuticals are also tightly correlated with the morphology of the MS, which may eventually affect the antitumor activity.[18] Therefore, PLGA MS with unique morphology properties have a significant potential as a TACE embolic agent, exhibiting high versatility.

The most common drug that is currently used in TACE is DOX. This drug is commonly used in anti-cancer therapy with clinical outcomes that are limited by its problematic cardiotoxicity, nephrotoxicity, and myelosuppression.[19] Although frequently used in TACE procedures, several reports revealed the development of increased resistance to DOX after performing embolization, mainly due to acute changes in the tumor microenvironment; these changes include increased acidity, multidrug resistance, and adaptation to cell death modulation.[20,21] Although monotherapy is widely used in oncology, it is well established that drug combinations are usually superior in terms of efficacy in HCC; hence, novel drug-delivery strategies that could support drug combinations are essential to improve TACE effectiveness.[22,23] Smart combinations would take advantage of the specific tumor microenvironment characteristics. Hypoxia-activated prodrugs are bioreductive compounds that are enzymatically transformed to be cytotoxic under hypoxic conditions. They have attracted increased interest as selective cancer treatments in recent years.[24] Tirapazamine (TPZ, 3-amino-1,2,4-benzotriazine 1,4-dioxide) is a hypoxia-activated prodrug that is preferentially toxic to hypoxic cells by generating DNA-damaging free radicals. A study performed in mouse models showed that TPZ injections that were followed by hepatic artery ligations led to synergistic tumor-associated deaths in HCC HBx transgenic mice.[25] Another study, conducted in a VX-2 tumor-bearing rabbit model, showed that the hypoxia-activated drug, TH-302, loaded in PLGA MS, was significantly superior to TH-302 injection, in addition to serving as an efficient candidate for TACE treatment of HCC.[26]

Taking that into consideration, TPZ and other hypoxia-activated prodrugs may transform embolization-induced hypoxia from a drawback to an asset, thus providing an adjuvant therapy to the current TACE practice to treat liver cancer. However, although the above-mentioned studies offer some advancement in the embolic MS fabrication or functionality, it ignores the effect of embolization on the tumor microenvironment, and lacks information regarding the physical and safety profile of the MS.

Despite the demonstrated advantage of the adjuvant TPZ therapy in improving the efficiency of liver cancer embolization therapy, there are many important unresolved topics that we address in the current study. We hypothesized that utilizing a dual combination of drugs (DOX and TPZ) that have a distinct mechanism of action may result in a stronger and synergistic effect against HCC. The potential synergy in the combination therapy was first determined in vitro in human and rattus cell lines under various oxygen conditions. Moreover, we hypothesized that the embolic MS morphology might also play a central role in the therapeutic effectiveness of embolization due to both, control over tissue perfusion and their ability to compress upon external pressure. Therefore, the effect of particle morphology on the drug loading and release profiles, as well as on compressibility properties were determined.

Microfluidic platforms were used to fabricate and characterize two different morphological types of embolic biodegradable MS: porous MS (P-MS) and non-porous MS (NP-MS) that are loaded with DOX and TPZ and are designed for TACE applications. Huh7, the Hep-G2 human HCC cell line, and N1-S1, the rat hepatoma cell line, were used to determine the optimal molar ratio of the drug combination and to investigate the potential synergistic effects under normoxia and hypoxia conditions in culture. An ex vivo model for embolism, referred to as the "EmboChip", based on the microfluidic device produced by 3D printing, was developed, and used. Using the EmboChip, we could test various effects on cells that were subjected to blockage of flow by the various types of embolic MS. Finally, a rat tumor-bearing

orthotopic model for HCC was established and used in a clinically similar TACE procedure. In this model we measured the safety of the embolic device, the capacity to perfuse drugs in the target tissue, and the overall anticancer effects of the combination therapy.

This work provides an embolic microsphere with unique morphology design, and advanced therapeutic applications. Our results indicated that the combination therapy, slowly released from the embolic device, exhibited better therapeutic outcomes compared with the single-drug treatments, while displaying a high safety profile. Moreover, MS porosity was found to be a critical parameter affecting drug release; it improves *in-vivo* efficacy and has a significant advantage of using porous MS compared with the non-porous version. Overall, these results imply that a TACE-based P-DOX-TPZ-MS might be a potential treatment modality for treating liver cancers and possibly additional malignancies that can benefit from TACE.

2. Results

2.1. DOX Cytotoxicity Critically Varies Under a Hypoxia and Normoxia Regimen in the HepG2, Huh7, and N1-S1 Cell Lines

In order to evaluate the effect of DOX on cellular viability under normoxic (21% O_2) and hypoxic (1% O_2) conditions, two human HCC cell lines, Huh-7, HepG2, and one rattus hepatoma cell line, N1-S1, were treated with increasing drug concentrations for 6, 12, 24, and 48 h. The generation of hypoxia was confirmed by measuring the HIF-1a via ELISA assay over time (Figure S1, Supporting Information). The effect of hypoxia on the cell viability values over different time points is summarized in Table S1 (Supporting Information). After 48 h, the cell viability of the HepG2 cell line declined to 77% when grown under hypoxic conditions, compared with normoxic conditions. The cell viability of the Huh-7 and N1-S1cell lines showed no statistical differences between hypoxia and normoxia. The dose-response curves showed the sensitivity of the treated cell lines in a time-dependent manner depicted in **Figure 1**a and the corresponding IC50 values are summarized in Table S2 (Supporting Information).

Under normoxic conditions, the IC50 of the Huh-7, HepG2, and N1-S1 cells to DOX decreased by 50-, 360-, and 23-fold, respectively, from a 6 to 48 h exposure time. However, when cells were grown under hypoxic conditions, a different trend was obtained for each of the cells. The IC50 values of Huh-7 and N1-S1 treated with DOX under hypoxic conditions increased from 1.7-fold to 4.2-fold, and 1.9-fold to 2.75-fold, respectively, over each time point exposure (represented as the relative H/N value in Table S2, Supporting Information). In contrast, when HepG2 cells were exposed to DOX under hypoxic conditions, the tolerance to DOX was reduced from 0.2-fold to 0.48-fold at each time point. Moreover, the hypoxic stimulation significantly enhanced VEGF secretion, compared with the normoxia regimen. VEGF was measured in normoxia and hypoxia in the cell condition mediums of Huh-7, Hep G2, and N1-S1 by ELISA assay after 48 h (Figure S2, Supporting Information). The expression of the VEGF levels was much higher compared with normoxia in all three cell lines. However, note that the highest increase was obtained in Huh-7 and N1-S1, with a 3.5-fold and 6.3-fold increase, respectively, from the basal level, compared with 2.5-fold in HepG2.

2.2. DOX and TPZ Exhibit a Cytotoxic Synergistic Effect that Inhibits N1-S1 Proliferation Under Hypoxia

Following the viability and cytotoxicity assay, which investigated the effect of DOX on human and rattus hepatic cancer cell lines under normoxic and hypoxic conditions, we aimed to evaluate the combinational effects of DOX and TPZ. DOX and TPZ (free forms) were tested in the rat hepatoma N1-S1 cell line under hypoxia (Figure 1b) and normoxia conditions (Figure S3, supporting information) induced for 48 h in order to evaluate and determine the optimal ratio for MS fabrication to be used in vivo. D/T, which specifies the molar ratio of DOX/TPZ assessed in vitro on the N1-S1 cell line, represents the combination of DOX and TPZ at various molar ratios. When DOX predominated in the combination therapy, adding TPZ resulted in a synergistic increase in cytotoxicity under the hypoxia regimen (Figure 1b). In contrast, when TPZ dominated, the increasing amount of DOX had a negligible effect in the combination therapy (Figure 1c), compared to a molar ratio of D/T = 1/1, which presented a cytotoxic synergistic profile. Subsequently, we evaluated synergistic combination therapy by calculating the combination index (CI) using CompuSyn software set up by Dr. Dorothy Chou in 2005.[27] The CI value provides a quantitative indicator to measure the extent of drug interaction, where a CI value of less than 1 indicates synergism; CI = 1 indicates an additive effect, and CI > 1 indicates antagonism.[28,29] Figure 1e summarizes the different treatment compositions, IC50 values, and the calculated CI. The IC50 values of DOX in the combination therapy were lower than those of free DOX treatment, with up to a 3-fold IC50 value dose reduction for doxorubicin. When TPZ dominated, a 2-fold IC50 dose reduction was found with the D/T = 1/2 group. However, no statistically significant difference was found in the IC50 values of free TPZ compared to D/T = 1/3. Figure 1d illustrates the plot of CI as a function of cell viability for the N1-S1 cell line treated with free DOX, free TPZ, and various molar combinations. A strong synergistic effect, characterized by a low CI value, was demonstrated in combinations of D/T = 3/1 and D/T = 2/1 (DOX dominant) with CI50 = 0.73 and CI50 = 0.56, respectively. However, antagonism (CI>1) was observed for the combination therapy, with TPZ being dominant. These findings suggest that D/T = 3/1 and D/T = 2/1 may be the best combination ratios for further investigation.

2.3. Fabrication and Characterization of Embolic MS

All polymeric MS used in this study were fabricated using a microfluidic focused flow chip for generating well-defined PLGA droplets as previously shown.[30] For fabricating non-porous (NP)-MS, the polymeric solution (PLGA in DCM) was introduced into a focused flow microfluidic chip to produce the MS. However, the porous morphology (P-MS) was obtained by first emulsifying the polymeric solution with 1% ABC solution as porogen, followed by fabrication in a microfluidic platform, as described in our previous work.[31] When DOX and TPZ were embedded into the polymer, a modified method of solid-in-oil-in-water (S/O/W)

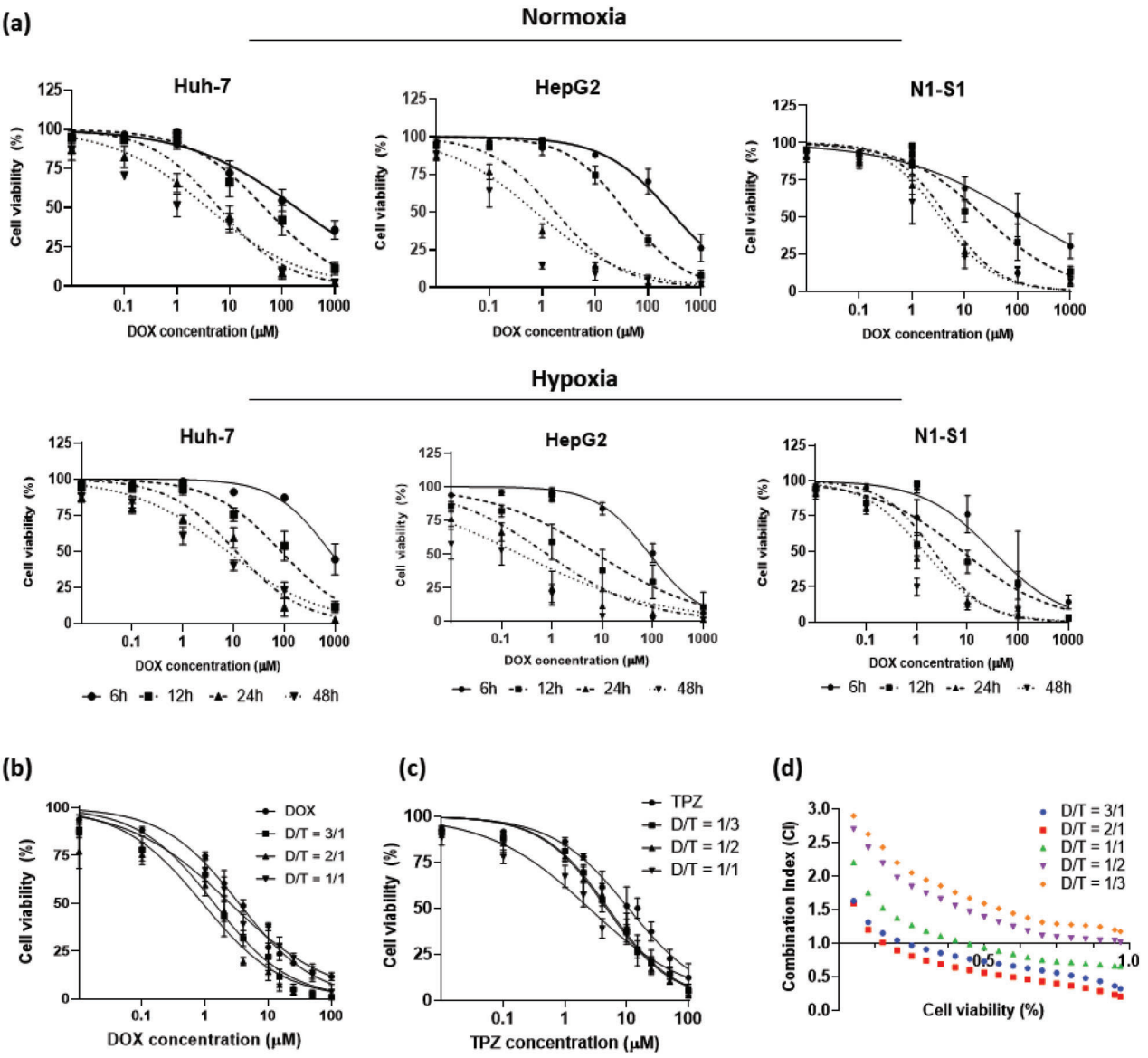

(e)

Drug combination	IC 50 (μm)	CI 50
DOX	3.412	-
D/T=3/1	2.07/0.69	0.73
D/T=2/1	1.54/0.77	0.56
D/T=1/1	1.10/1.10	0.93
D/T=1/3	2.43/4.87	1.56
D/T=1/2	3.17/9.51	1.38
TPZ	10.27	-

Figure 1. Effect of DOX treatments on cell viability under normoxia/hypoxia regimen and synergistic cytotoxicity effect of TPZ and DOX represented in dose–response curves over time. a) The cytotoxity of DOX in the Huh-7, HepG2, and N1-S1 liver cancer cell lines treated with increasing concentrations

was used prior to fabrication in the microfluidic system. In contrast with blank polymeric MS fabrication, a preliminary step of solid film preparation was carried out to effectively embed these hydrophilic drugs of interest. Afterward, this film was dissolved in DCM and emulsified with 1% ABC, followed by the formation of a second emulsion in the microfluidic chip. The achieved solidified MS are characterized by a high homogeneity and a low polydispersity index (**Figure 2**a).

The mean diameter and surface morphology of the PLGA MS were studied by both the particle size analyzer and SEM, which revealed a spherical shape. MS were characterized by a narrow size distribution, with an average diameter size in the range of 42–48 μm.

The particle diameter size was determined based on both, rat blood microvessels diameter to be occluded (to avoid harmful adverse events, e.g. thrombus) and by the special microcatheter used in the procedure in vivo to ensure continuous flow of the MS.[32,33]

The average EE values of DOX and TPZ were over 60% in all cases. The mean DC values are shown in Figure 2b. The obtained molar ratios of NP-DOX-TPZ and P-DOX-TPZ were 2.11:1 and 2.05:1, respectively. Moreover, the elastic characteristics of the embolic MS were tested using a microfluidic chip with a converging channel simulating the blood vessel structure (Figure 2c). P-MS were able to flow along the converged channel to the narrow end of the tunnel, showing a mean diameter size reduction of 20%. In contrast, the NP-MS had no compressibility and thus blocked the flow channel.

After determining the optimal cytotoxicity and the synergistic combination index (CI) between DOX and TPZ (2:1) in the free-form drug, the CI was investigated with both MS morphologies in the N1-S1 cell line. Figure 2d illustrates the CI of D/T 2:1 polymeric MS calculated using CompuSyn software. Although both particles' morphologies exhibited synergistic properties (CI<1), porous MS (Figure 2d left) exhibited a better synergistic profile compared with the non-porous MS (Figure 2 right). The CI values of the drug-loaded MS were higher than those obtained in the free-form drug cytotoxicity assay. Finally, the viability of the N1-S1 cell line with blank MS was also examined and revealed no cytotoxicity (data not shown).

2.4. In Vitro Drug Release and Biodegradation of DOX-TPZ MS

A specially designed 3D-printed microfluidic chip was fabricated to evaluate and monitor the release and the degradation rate of drug-loaded MS over a period of 14 days (**Figure 3**).

The chip was connected to a syringe filled with PBS release medium adjusted to two different pH values: a physiological pH of 7.4 to mimic the environment of the bloodstream, and a pH of 6.2 to simulate the acidic tumor microenvironment. When comparing both MS morphologies, the cumulative release in the first 48 h shows a statistically significant difference in the release patterns (Figure 3a,b), as well as the total drug release amounts (Figure 3c,d). In all experiments, we found that DOX had a faster, and more extensive release than TPZ, with an accelerated rate in acidic conditions. Regarding the porous MS, in the first 2 days under a pH of 6.2, DOX showed a sharp burst release reaching ≈35%, almost double that at pH 7.4, whereas TPZ showed ≈15% and 8% of drug release, respectively. In comparison to the non-porous morphology, the DOX release amount after 2 days at pHs of 7.4 and 6.2 reached ≈13% and ≈20%, respectively, and TPZ obtained values of ≈6% and ≈11%, respectively. Additionally, the release pattern differs between the two MS morphologies in the first 48 h. Whereas the porous morphology exhibited a sharp burst release in the initial phase, the non-porous morphology displayed a more moderate one. After 14 days, the DOX and TPZ release profiles reached a plateau and the overall drug releases from both MS morphologies were higher at acidic pH 6.2 than it was at the physiological pH of 7.4 (Figure 3c,d). As for P-DOX-TPZ MS, under a pH of 7.4, DOX and TPZ reached ≈37% and ≈17% of drug release, respectively, whereas at a pH of 6.2, they reached ≈63% and ≈34% of drug release, respectively. However, NP-DOX-TPZ MS achieved lower drug release values for both drugs. The release amounts of DOX and TPZ were ≈31% and ≈14%, respectively, at pH 7.4, and ≈48% and ≈21%, respectively, at pH 6.2. In addition to the release profile, the degradation rate of the drug-loaded MS was evaluated for 14 days utilizing both, a microfluidic dissolution chip using media containing 50% (v/v) FCS with PBS and via in vivo study. Regarding the in-vitro assay, both MS morphologies were observed by SEM during the investigation period at days 0, 7, and 14 (Figure 3e,f). The P-MS morphology degradation showed that at day 0 the particles exhibit a round shape with a thickened wall polymeric structure. At day 7, at pH 6.2, a reduction in thickness of the particle structure was observed and the pore size increased, compared with MS evaluated at pH 7.4. Moreover, a mild deformation of the round shape was noted. By day 14, at a pH of 6.2, the MS morphology changed from spheres to irregular shapes with larger pores. The formation of multiple enlarged pores was observed on the particle surface as well as in the core. The NP-MS on day 0 were smooth and spherical. At day 7, at pH 6.2, the particle exhibited a coarse surface texture with small pores on the outer shell, in comparison with pH 7.4, which induced smaller pores with a lower volume. On day 14, a semi-porous structure with an irregular round shape can be seen in the MS evaluated at pH 6.2, compared with the MS at pH 7.4, which exhibited a round shape with a few pores on the surface. Furthermore, a particle size measurement revealed a size reduction of ≈15% and ≈10% from the initial mean diameter of the porous and the non-porous MS, respectively. The data obtained from the in vivo study found to be in correlation with the data obtained in-vitro (Figure S6, Supporting Information). On day 0, the porous MS exhibit round and rigid structure. At day 7, a reduction in size can be seen in addition to a surface pore enlargement. By day 14, the porous net reduced

under normoxic and hypoxic conditions for 6, 12, 24, and 48 h. The average and standard deviation are shown for each treatment condition. Moreover, the cytotoxicity of free DOX and free TPZ at various molar ratio combinations was measured over 48 h under a hypoxic environment. b) DOX dominates, c) TPZ dominates; d) The plot illustrates the combination index (CI) as a function of cell viability for N1-S1 cells exposed to different molar ratios of free DOX and TPZ. (Normoxia is in the supporting information section.) e) A table summarizes the different free drug combinations, IC50 and CI50 of the N1-S1 cell line after 48 h of incubation. All data represent the mean (symbols) ± standard deviation (SD, error bars) from at least 5 independent experiments.

(a)

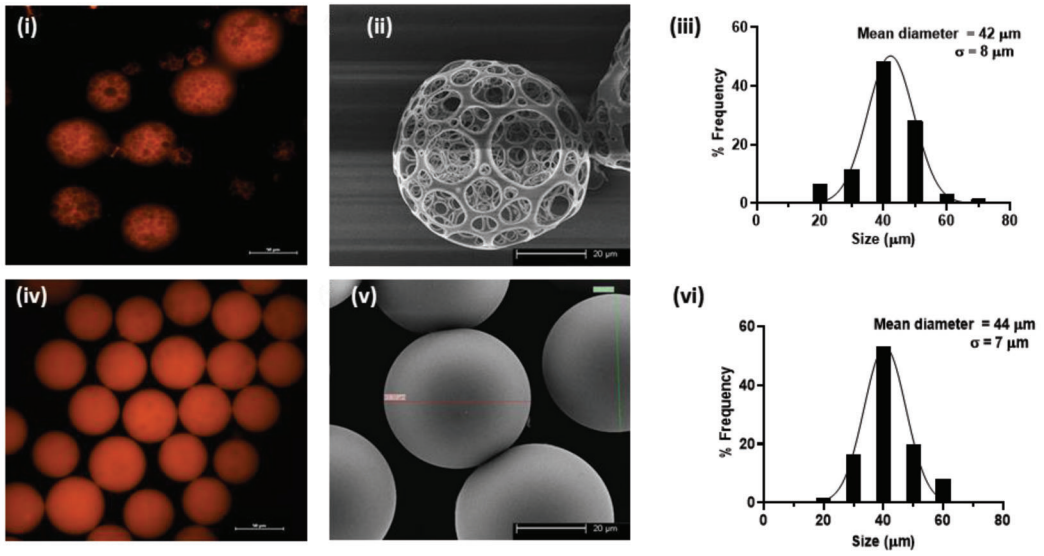

(b)

Formulation	Mean diameter (µm)	DOX encapsulation efficiency (EE%)	DOX Drug content (DC%)	TPZ encapsulation efficiency (EE%)	TPZ drug content (DC%)	Real molar ratio of DOX/TPZ
NP-MS	46±4	-	-	-	-	-
P-MS	48±5	-	-	-	-	-
P-TPZ MS	43±7	-	-	68.7±0.9	6.33±0.7	-
P-DOX MS	41±8	62.2±0.7	7.2±0.8	-	-	-
NP-DOX-TPZ MS	46±6	69.2±0.6	7.9±0.3	74.2±0.2	7.7±0.6	2.1:1
P-DOX-TPZ MS	44±5	60.3±1.3	7.3±0.6	66.3±0.74	6.14±0.15	2.05:1

(c)

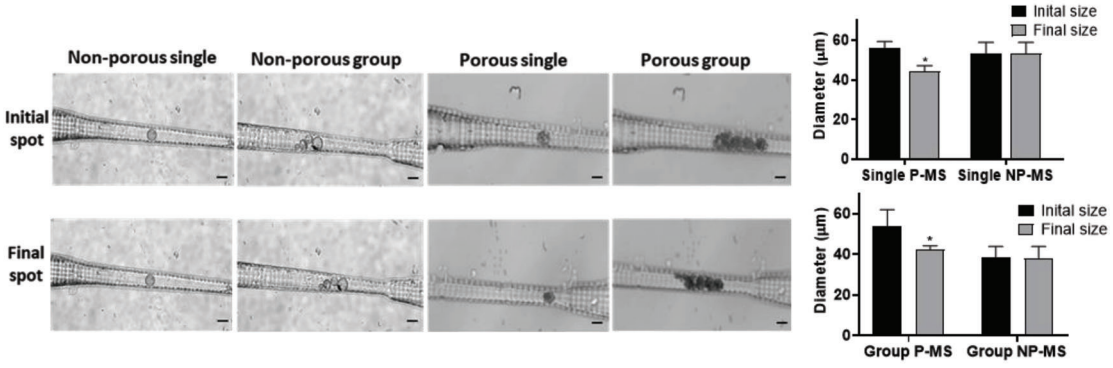

(d)

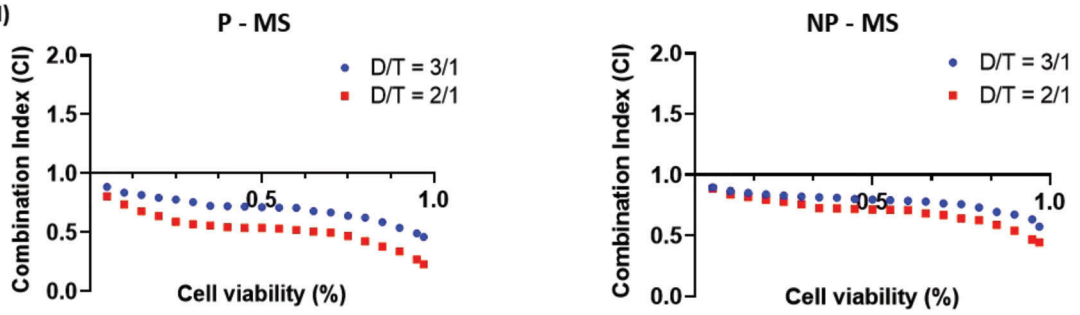

Figure 2. Physicochemical characterizations and combination index of fabricated porous and non-porous MS. a) Morphology examination and a histogram plot of P-DOX-TPZ and NP-DOX-TPZ PLGA MS observed by scanning electron microscopy (SEM), a particle size analyzer, and a fluorescence

substantially, and the MS morphology characterized overall with pores enlargement and size reduction of 10–15%. Finally, no significant difference was found in the release profile of the MS embedded with only DOX or TPZ (data not shown).

2.5. In Vitro Embolization Using the EmboChip

In order to mimic the embolic process that occurs in vivo using the optimized MS, we studied their capacity to block fluid perfusion and induce cytotoxicity in vitro using the "EmboChip", a designated microfluidic chip that mimics perfusion in nourishing capillaries. The device was manufactured using 3D printing and soft lithography (**Figure 4**a,b).

In this device, we administered a liquid medium, stained with Evan's blue fluorescence dye, at a flow rate of 20 μL min^{-1} into the main chamber, with or without the infusion of embolic particles (Figure 4c). When NP-MS was injected, the convergent channel was completely occluded and the medium flow into the chamber halted 15 minutes after perfusion of <100 μL. However, when porous MS were injected into the EmboChip, the tunnels were partially occluded, allowing the blue medium to also flow into the main chamber)194 μL (, on average, over the same time course of 15 min. Compared to the embolic MS tested, the control assay exhibited a linear fluid flow, and over 15 min, a total of 300 μL flowed into the main chamber. Following the establishment and calibration of the EmboChip parameters, and 24 h after seeding the N1-S1 cell line inside the main chamber, the *in-vitro* embolization was performed using both particle morphologies, with and without drugs (Figure 4d). Note that with blank and drug-loaded NP-MS, the medium flow stopped after 20 min due to acute blockage and elevated the fluid pressure in the chip. After 48 h, cells were removed and washed for analysis of cell viability. Compared to the control, the EmboChip cells treated with blank NP-MS and P-MS had a cell viability of 65% and 74%, on average, respectively (Figure 4e). EmboChip cells treated with drug-loaded NP-DOX-TPZ and P-DOX-TPZ MS had a cell viability of 53% and 24%, on average, respectively. In these studies, porous dual drug-loaded MS decreased the cell viability threefold levels, compared with the blank MS, and by more than twofold, compared with the non-porous drug-loaded MS. This suggests that the dual drug therapy MS had a significant impact on cell cytotoxicity.

2.6. In Vivo Efficacy Studies for Drug-Loaded Microspheres and Drug Biodistribution

The in vivo synergistic antitumor effects of the DOX-TPX drug-loaded MS were studied in the following groups: control (sham group), blank NP-MS, blank P-MS, P-TPZ MS, P-DOX-MS, NP-DOX-TPZ-MS, and P-DOX-TPZ-MS. All tumor-bearing rats were treated with selective left hepatic artery embolization with the above-mentioned MS using a fluoroscope machine and digital subtraction angiography (DSA) imaging to confirm that the embolization of the tumor-supplied arteries was successfully achieved. Ultrasound-guided intrahepatic tumor cell transplantation in rat liver, catheterization via the carotid artery, and liver tumor transcatheter embolization in rats are depicted in **Figure 5**a–i.

Figure 5j demonstrates a macroscopic observation of rat livers after euthanization. The negative control group was excised; all rat livers had tumors with varying sizes and exhibited a normal morphology after they were harvested. No statistically significant differences were found in tumor volumes prior to the embolization procedure. The antitumor effects of drug-loaded polymeric MS investigated 10 days post-treatment are depicted in Figure 5k–n. Figure 5k,l shows the tumor volume of different treated groups monitored by the HF-US machine during the study follow-up. Compared to the control group, rats that were treated with MS exhibited an expected inhibition of tumor growth, whereas the sham group exhibited the highest tumor volume (2.4 cm^3) compared to other treated groups. Groups treated with NP-MS and P-MS exhibited slower growth rates than that of the sham group, whereas the blank P-MS presented a better tumor response, compared with NP-MS, with a tumor volume of 1.7 and 2 cm^3, respectively. Nevertheless, the tumor inhibition efficiency of the P-DOX-TPZ-MS group was found to be superior to that of other embolic MS treatments. The volumes of liver tumors treated with P-DOX-TPZ MS (0.9 cm^3) were significantly lower than the other drug-loaded MS groups, P-DOX-MS (1.4 cm^3), P-TPZ-MS (1.2 cm^3), and NP-DOX-TPZ-MS (1.2 cm^3). Interestingly, the tumor volume of rats treated with drug-loaded DOX-TPZ MS showed a similar decrease during the first 4 days after embolization. However, from day 6, a significant gap in tumor volume inhibition was detected in the group treated with drug-loaded MS and specifically in the P-DOX-TPZ MS group. In addition, the drug concentrations in the tumor and normal liver regions were determined 10 days post-embolization (Figure 5m,n). The distribution ratios of DOX and TPZ (liver tumor/normal liver) were found to be significantly higher in the porous morphology group (P-TPZ, P-DOX, and P-DOX-TPZ) than in the non-porous morphology (NP-DOX-TPZ) group. The mean ratios of the drug concentrations in the tumor region and in the normal liver when using P-DOX and P-TPZ groups were 5.2 and 7.8, respectively. Note that despite a lower drug-loading value in the porous MS, compared with the non-porous MS, the drug tumor value and the drug concentration ratio were higher in the porous MS. The mean concentration of drugs in the tumor was 1.8-fold higher, on average, in the P-DOX-TPZ-MS group than in the NP-DOX-TPZ-MS group. In particular, the drug mean concentration ratio of DOX and TPZ in P-DOX-TPZ-MS was 6.6 and

microscopy image. Panels (i–iii) are fluorescence images, a SEM image, and a size distribution histogram of P-DOX-TPZ MS, respectively. Panels (iv–vi) are fluorescence images, a SEM image, and a size distribution histogram of NP-DOX-TPZ MS, respectively. b) A summary of the mean diameter, encapsulation efficiency (EE), and drug content (DC) values of the different fabricated MS. Data are presented as the mean ± SD ($n = 3$). c) Particles elastic/deformation ability test in microfluidic chip. Porous and non-porous polymeric MS (single and grouped) was introduced under a constant flow into a microfluidic device consisting of a converged tunnel (500 μm to 40 μm) mimicking a blood vessel design to test the particles' deformation ability. Porous MS managed to flow along the converge tunnel and showed compression ability with up to a 20% reduction in diameter size (upper and bottom graphs), compared with the non-porous MS that constrained and showed no compression properties. The scale bar is 50 μm. d) Combination index (CI) plot as a function of cell viability for N1-S1 cells treated with P-MS (left) NP-MS (right) loaded with DOX and TPZ under varying molar ratios. *$p < 0.05$.

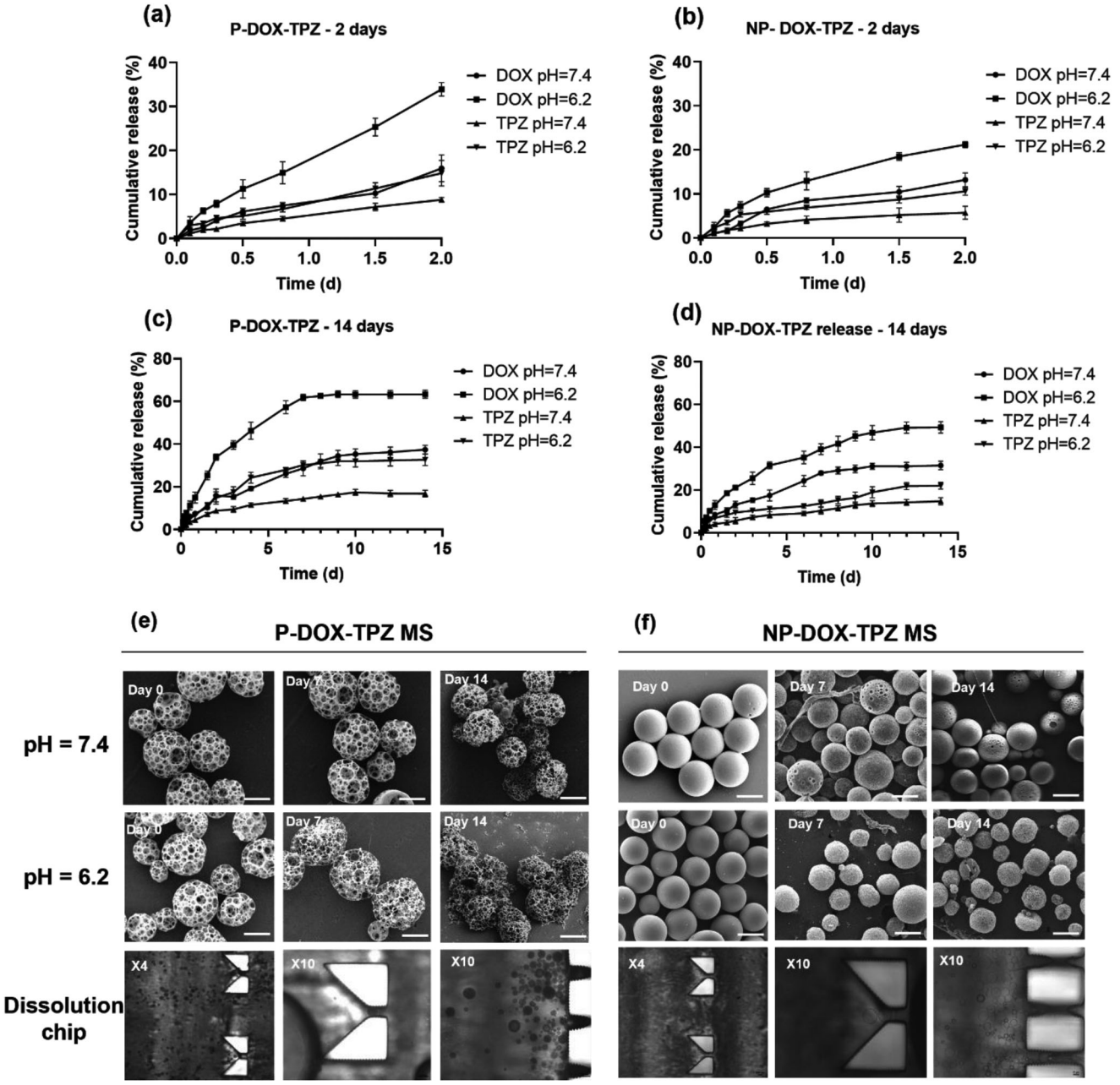

Figure 3. In vitro degradation and cumulative drug release profiles. a–c) P-DOX-TPZ (2:1) and b–d) NP-DOX-TPZ (2:1) MS. The drug release and the degradation experiment were performed using a 3D-printed microfluidic chip over a 14-day period under pHs of 7.4 and 6.2. The results are expressed as the mean ± SD (n = 3). Scale bar in (e) and (f) is 40 µm.

9.0, respectively, whereas the DOX and TPZ mean concentrations in NP-DOX-TPZ-MS were 2.9 and 3.05, respectively.

2.7. Histology and Immunostaining

Histopathology was studied by observing the hematoxylin and eosin (H&E), Caspase-3, CD-31, and Ki-67-stained slides under an optical and fluorescence microscope (**Figure 6** and Figure S5, Supporting Information). As shown in Figure 6a, the necrosis of the liver tumor section was examined by H&E staining.

No necrotic areas were observed in the negative control, or the sham group compared to the MS-treated groups. Among the different treatment groups, P-DOX-TPZ-MS displayed the largest necrotic area and the lowest cell density. Additionally, Caspase-3, Ki-67, and CD-31 stainings were performed to evaluate the apoptosis rate, antitumor proliferation effectiveness, and angiogenesis, respectively. The control (sham) group showed a high cell proliferation index (74%); the brown nuclei were Ki-67

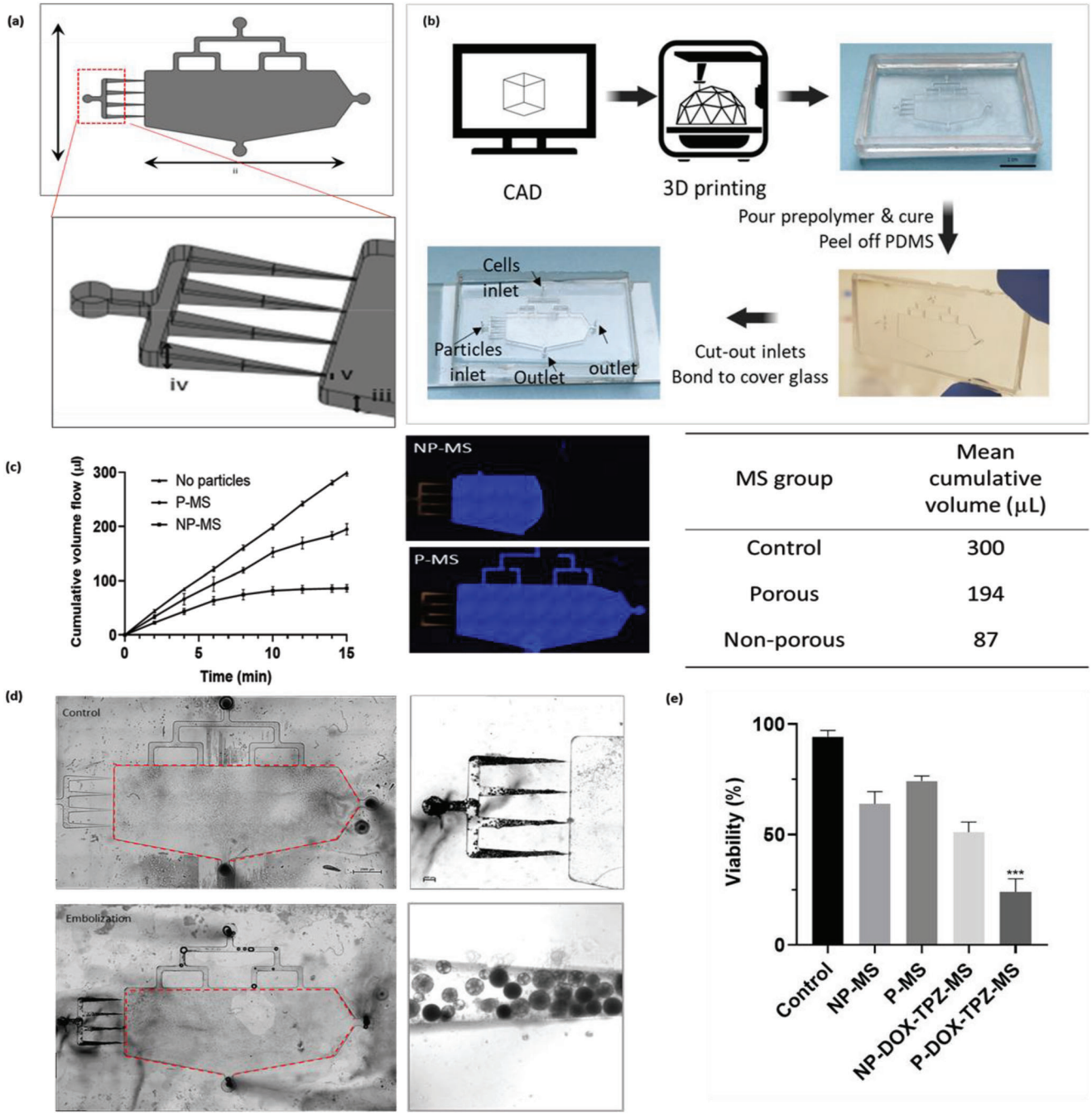

Figure 4. Fabrication process of EmboChip followed by an *in-vitro* embolization with porous and non-porous MS. a) Embo-chip microfluidic overhead and side view schematic illustration. The length (i) is 18 mm, main chamber width (ii) is 25 mm, and the height (iii) is 500 µm. The tunnels initial height (iv) is 500 µm and converges to a minimum height (v) of 50 µm. b) Fabrication of a PDMS-based microfluidic device (EmboChip) by a 3D printed recyclable mold. Followed CAD design and printing process, the PDMS resin is poured into the pattern framework. After an overnight crosslinking process, the PDMS was gently peeled from the framework, tubed and went through an O_2 plasma bonding machine for final glass bonding. The device contains one microsphere entrance inlet, one cell inlet, and two outlets. c) Cumulative volume of release media flew through particles. P-MS and NP-MS introduced into EmboChip under constant and continuous flow rate. Fluid flow stopped after 15 min on average in NP-MS with 87 µL fluid flow while in the group of P-MS it achieved 194 µL. Fluid in P-MS group continued to flow for 48 h (not shown). Dead volume in the tube excluded. d) In-vitro embolization performed in EmboChip microfluidic device. e) Assessing viability of N1-S1 cell line following in-vitro embolization procedure conducted with varying particles (Blank and drug-loaded MS) over 48 h period. P-DOX-TPZ MS exhibited the highest cytotoxicity among tested MS groups. $n = 3$.

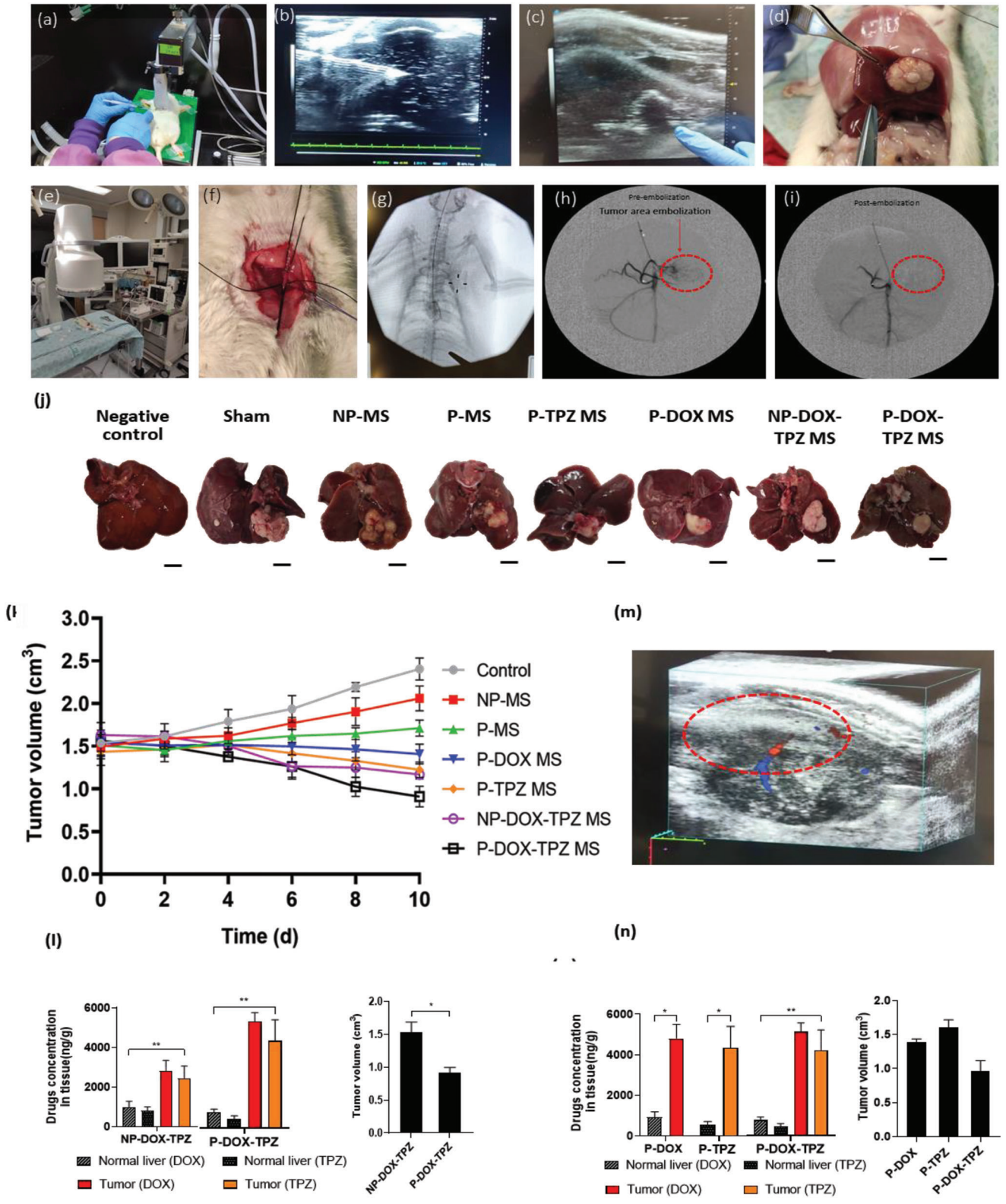

Figure 5. Establishment and development for induction of orthotopic HCC model in rat and antitumor activity and follow-up of rats' liver post embolization treatment using porous and non-porous MS. (a+b) Ultrasound (US)-guided intrahepatic injection of N1-S1 tumor cells. c) US follow-up showing a tumor on day 12. d) Dissection of the rat revealed a normal liver parenchyma and a visible single tumor at the induction site. Following rat anesthesia (e), the left carotid artery was exposed (f) and the microcatheter was gently inserted (g). h) To validate the proper position of the microcatheter, a contrast agent was slowly injected. i) To ensure embolization was completed, a contrast agent was injected afterward, but it could not be detected in the tumor area, which demonstrates that this method could eliminate tumor vascularity. j) Rat liver macroscopic observation. The scale bar = 1 cm. k) Rat liver

positive, compared with lower values in all other treatment groups; P-DOX-TPZ-MS showed the lowest levels of proliferation (11%) (Figure 6b). In addition, the indices for Caspase-3, which are visible by the brown-stained apoptotic zones in the control (sham), NP-MS, P-MS, P-DOX-MS, P-TPZ-MS, NP-DOX-TPZ-MS, and P-DOX-TPZ-MS groups were 12, 23, 37, 49, 55, 59, and 75%, respectively (Figure 6c). Furthermore, the expression of CD-31 was significantly lower in the tumor treated with P-DOX-TPZ MS compared to other treated groups as shown in the histology examination and MVD analysis (Figure S5, Supporting Information), and overall imply on anti-angiogenic effect of the combined treatment. Bright-field and fluorescence images (DAPI fluorescence (blue) represents the cell nuclei, whereas Cy3 fluorescence (orange) represents DOX) of porous and non-porous DOX-TPZ-MS groups were taken (Figure 6d–i), showing the fluorescence's successful incorporation into the tumor-feeding arteries. Both particle groups are located near the tumor area; however, only the P-DOX-TPZ-MS group showed an orange color, indicating DOX (Figure 6h) in the tumor zone, compared with NP-DOX-TPZ-MS, which showed none (Figure 6e).

2.8. Biosafety

The biosafety of fabricated MSs was examined by histological H&E staining on the main peripheral organs including the heart, kidney, lung, and spleen, in addition to analyzing the blood biochemical indices (**Figure 7**).

Based on the histological analysis, there was no obvious tissue damage or inflammation lesions in the examined organs, compared with the control group (blank MS). Furthermore, rat serum was obtained to measure the main blood biochemical indices during the treatment procedures. Two informative liver function indices, alanine aminotransferase (ALT) and aspartate transaminase (AST), showed an increase on the first three days, followed by a gradual decrease to the basal level afterward by day 10 (Figure 7b,c) For kidney monitoring, the values of creatinine (Cr) and blood urine nitrogen (BUN) were found to be stable during the study (Figure 7d,e). Taken together, these results indicate that the DOX-TPZ MS used in this study had a good biosafety profile.

3. Discussion

This comprehensive study introduces a newly developed drug-eluting embolic platform based on porous PLGA MS; it has many advantages over the existing embolism solutions. For example, the designed MS exhibit elasticity and mechanical compressibility that improve their application and localization in the intravascular space. Moreover, the platform is suitable for slowly releasing drug combinations, and due to its porosity, it maximizes drug perfusion into target tissues while minimalizing adverse acute tissue stress. An important feature of our approach is the leverage of the specific physiological niche as it exists in the embolic tissue, thus incorporating a hypoxia-activating prodrug that enhances activity in the elevated hypoxic microenvironment.

The current state of the art in TACE treatments is the use of DOX as the main chemotherapy. Here we compared DOX therapy as a monotherapy, to a combination with TPZ. As a first stage, we explored whether cancer cells respond differently to DOX therapy under varying O2 conditions. Three liver cancer cell lines, HepG2, Huh7 (human origin), and N1-S1 (rattus origin), were exposed to various concentrations of DOX for different durations under normoxia and hypoxia regimens. Of the three cell lines, HepG2 was found to be the most sensitive cell line in comparison with Huh7 and N1-S1, which showed higher tolerance, which was also demonstrated in other reports.[34,35] There is some discrepancy in the IC50 values of the human cell lines, Huh-7 and HepG2, which were found in other studies. For example, Francesca Capone et al. found HepG2 cells to be more sensitive to DOX treatment compared with Huh7 cells, whereas Chang et al. reported that the Huh7 cell line was as sensitive as HepG2,[36] and Terence Kin-Wah Lee et al. showed that Huh-7 was more sensitive to DOX than was the HepG2 cell line.[37] However, in all cases in which DOX affected the cells, the cell heterogenicity emphasizes the need to measure cytotoxicity under standard and fixed conditions throughout a given study.

A clear trend of time dependence was found in the cytotoxic activity of DOX. The IC50 values of DOX were lower with the extended duration in cell exposure both in the normoxia and the hypoxia regimens. This phenomenon correlates with other reports and can be explained by the PK-PD relationship.[38] For example, a 4–18-fold decrease in DOX IC50 was reported for the Huh-7, HepG2, and SNU449 cell lines from 24 to 48 h.[39] In HepG2, the IC50 value decreased in hypoxia over time, as opposed to the Huh7 and N1-S1 cells where the tolerance to DOX increased, compared with the normoxic conditions. In addition, inducing hypoxia on the cells resulted in various responses regarding the cell line's viability (Table S1, Supporting Information). More specifically, the viability of HepG2 cells decreased to 77% under hypoxia, whereas the vitality of the Huh7 and N1-S1 cell lines was shown to be unaffected by this regimen. These results indicate that hypoxia enhances the resistance of cells to DOX, which could be explained by the different levels of HIF1, and the VEGF proteins detected in the three cell lines. Hypoxia promotes HIF-1, which is a master regulator of oxygen homeostasis in cells via stimulating the HIF signaling pathways. Under normal conditions, HIFs are constantly expressed and destroyed, but under hypoxia, they are stabilized.[40] In hypoxia, the cancer cell lines' tolerance to chemotherapeutic drugs might change, thus inducing resistance to chemotherapy, depending on the cell origin, type, and the drug agent.[41,42] The Huh7 and N1-S1 cells exhibited the highest protein level of HIF1a, compared with HepG2 cells, suggesting that these cells could better adapt to a hypoxic environment, compared with HepG2.[43] Another important way of activating HIF1a is by promoting the transcription of VEGF, which functions as a key driver of tumor development and hypoxia environment adaptation.[44] Although the VEGF levels were comparable under the normoxia regimen after 48 h (Figure S2, Supporting Information), they were significantly elevated under the hypoxia regimen in the Huh7 and N1-S1 cell lines (fourfold,

tumor measurement over 10 days following embolization. l) US image of a rat liver tumor during follow-up. m) Comparison of the DOX and TPZ tissue distribution in liver healthy parenchyma and the liver tumor region and the effect on the tumor volume 10 days after embolization using NP-DOX-TPZ, P-DOX-TPZ, P-DOX, and P-TPZ MS.

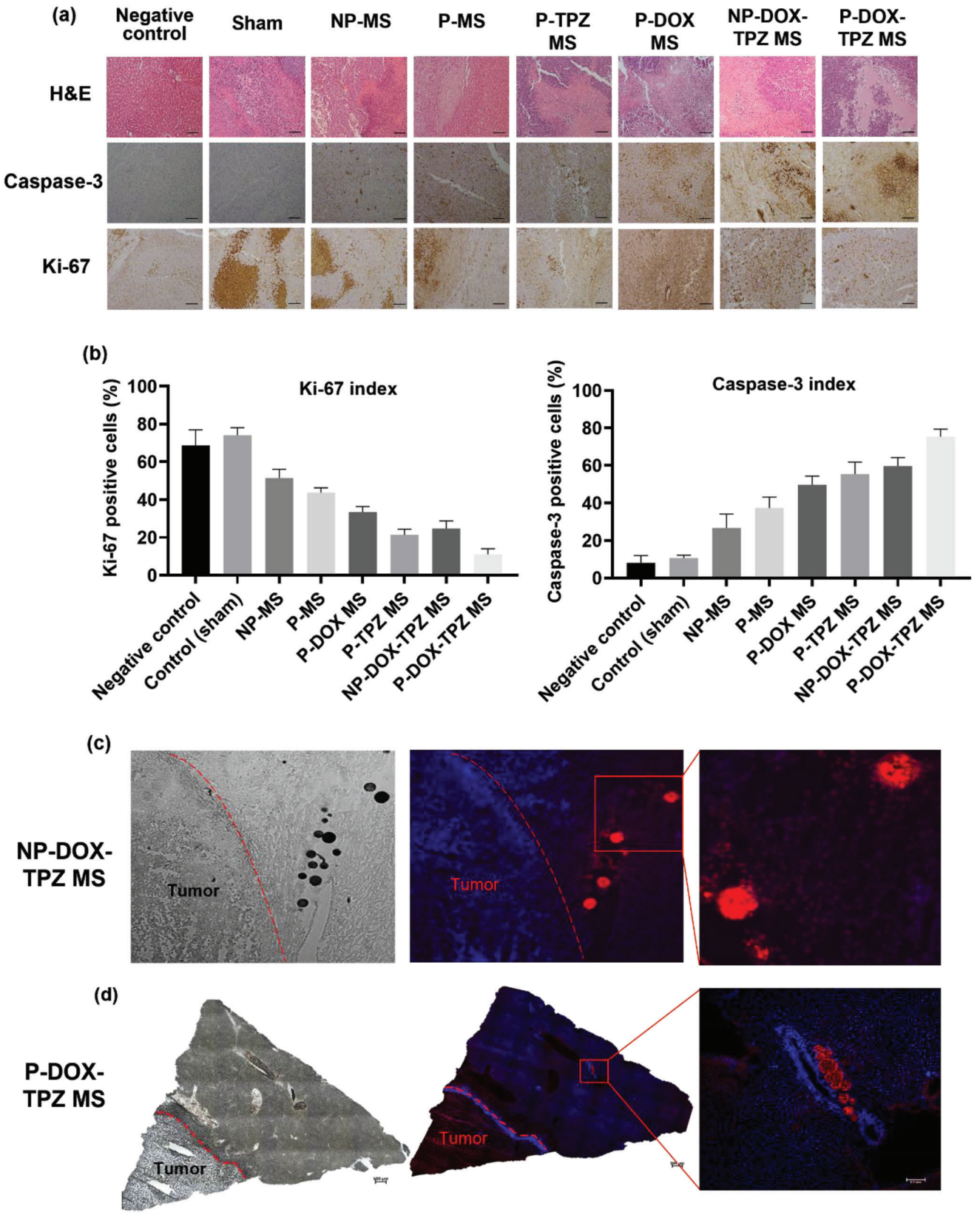

Figure 6. Tumor histology analysis in rats 10 days following embolization therapy. a) Representative images of immunohistochemical staining for H&E, caspase 3, and Ki-67 on tumor tissues. Cells that are caspase-3 and Ki-67 positive are denoted in brown. b) Index of positive cells for Ki-67 (left) and

on average), compared with HepG2 (2-fold), suggesting a better adaption and proliferation ability under hypoxic conditions.[45] Possibly some variance between our results and previous reports is the mode of hypoxia induction, which could occur either by a chemical agent ($CoCl_2$), as done by other studies, or by specific gas conditions using a mixture of 1% O_2, as we used in this study.

The important observation associated with the reduced activity of DOX in hypoxia can partially explain the modest clinical outcomes of the current TACE therapies that use DOX as the primary active compound in liver embolism. The hypoxic niche that is induced in the liver upon embolism possibly limits the activity of the drug; therefore, there is a clear rationale to use drug combinations, and especially to select drugs such as TPZ, which will be more potent under hypoxia conditions.

The effects of DOX and TPZ, combined in varying ratios, were measured in cells in order to determine whether there are additive or synergistic effects. Figure 1b–e illustrates that TPZ, combined with DOX, had a stronger synergistic effect on inhibiting the proliferation of N1-S1 cells. When supplied simultaneously in their free form, DOX (dominant) synergizes with TPZ over a range of combination ratios with the optimum at a ratio of D/T = 2/1, which led to the lowest CI value (0.53). There are several suggested mechanisms of action for DOX in cancer cells. DOX can intercalate into the DNA base pairs and inhibit topoisomerase-II. Moreover, it was shown that DOX increases the production of free radicals and oxidative damage to cellular components, leading to cell death and senescence with alternative pathways, which could result in broad effects on various cell types.[46,47] However, TPZ is a hypoxia-activated pro-drug that can induce DNA-damaging radicals, and interfere with intracellular pH and energy metabolism, which can consequently lead to cell damage even in low doses under hypoxic conditions or higher dosages in normoxia (Figure S3, Supporting Information).[48,49] Moreover, the generated radical species might interact with DNA, producing single- and double-strand breaks, leading to topoisomerase II poisoning, either by direct damage from TPZ or by the radicals generated on the DNA molecules. Therefore, the synergism, possibly induced by the overlapping mechanism of actions of the two drugs, concomitantly amplifies DNA damage and suppresses DNA repair mechanisms.[50,51]

In order to efficiently deliver the optimal anticancer DOX and TPZ combination, we incorporated the drugs into the degradable scaffold of porous PLGA MS assuming that this could enhance drug release into the gradually occluded tissue prior to full blockage of flow. The PLGA MS were fabricated using microfluidics and were loaded with the synergic drug ratio, as identified in the cell assays. The MS were well characterized and exhibited uniform physicochemical properties (Figure 2a). The enhanced therapeutic effects may eventually lead to better clinical outcomes as a result of the higher drug release rates and the reduced prolonged tissue stress associated with acute embolism. Possibly the TACE procedure could be repeated, if needed, which can also potentially prolong its activity. The drug loadings of both drugs in the porous MS were higher, compared with traditional synthesis methods.[11] This is due to our synthesis method, which uses microfluidics instead of batch synthesis, which often leads to nonlinearities and system fluctuations.[52] Interestingly, the drug EE values of TPZ were higher than those of DOX, which could be explained by the solubility differences between these drugs. Compared to TPZ, DOX HCl is more hydrophilic; thus, a PLGA polymer with a higher lactic acid ratio (75:25) might limit its loading due to it leaking out of the external aqueous phase during the MS fabrication process.[53] Possibly the use of a more hydrophilic PLGA (e.g., 50:50) might increase DOX entrapment in the polymeric matrix. Based on The International Union of Pure and Applied Chemistry (IUPAC) porous materials characterization, the porous MS used in this study categorized under the term of macropores (pore size > 50 nm).[54] The pore size was determined based on the results of this study and our previous work.[31]

Beyond the ability to load drugs in the porous MS, other important advantages of porous structures, compared with the dense rigid ones, were revealed. In terms of mechanical properties, the porous morphological MS were found to be elastic and more compressible than the non-porous MS, as measured under flow that simulates the convergence of blood vessels inside a microfluidic chip. Porous materials are characterized by open inner structures that enable compression, given sufficient pressure.[55] The compressibility and flowability are highly important for clinical practice since these characteristics might substantially ease the application of the particles during embolism. A smooth passage through converged cavities can allow the localization of the particles proximally to the target tumor site and occlude small blood vessels. Moreover, the porous MS, due to their low density and good flowability, could potentially prevent microcatheter blockage which is often a problematic issue in clinical procedures.[56]

The overall performance of the drug-loaded porous PLGA MS was thoroughly examined in cell assays. The combination index was measured and found to be similar to what we measured with the free drugs, but with slightly higher values, which may be due to the slow release of the drugs from the MS.[57] The slightly lower CI values of porous MS, compared with the non-porous ones, were mainly due to different release patterns and rates from the PLGA matrix. Porous materials are characterized by open structures that allow a greater flow of liquid that can reach and dissolve the entrapped drugs into the medium more quickly, compared with the non-porous MS (Figure 2d).[58]

The biodegradability and drug release of PLGA P-DOX-TPZ and NP-DOX-TPZ MS were determined using our 3D-printed dissolution chip, which was detailed in our previous paper.[59] As shown in Figure 6, both MS morphologies exhibited a sustained drug release profile that reached a plateau phase after 14 days. A careful analysis of the first 48 h revealed that the initial release profile of both MS morphologies was different. An initial steeper rise in drug release ("the burst effect") was obtained in the porous morphology, compared with the non-porous one, which exhibited a gradual rise. Moreover, interestingly, even though the non-porous MS had higher drug loadings, the release

Caspase-3 (right) in each treated group calculated as the ratio of positive cells to the total cells ($n = 5$). c,d) Representative images of tumors that were treated with non-porous (d) and porous (e) DOX-TPZ MS. Cross section bright field microscopy images of rat liver after embolization show particles in feeding arteries near the tumor area. Fluorescence images show PLGA MS in the tumor blood arteries that contain DOX. DAPI- blue. DOX- orange. The scale bar in a) is 100 µm. The scale bar in d) left and middle is 500 µm. Scale bar in d) right image is 100 µm.

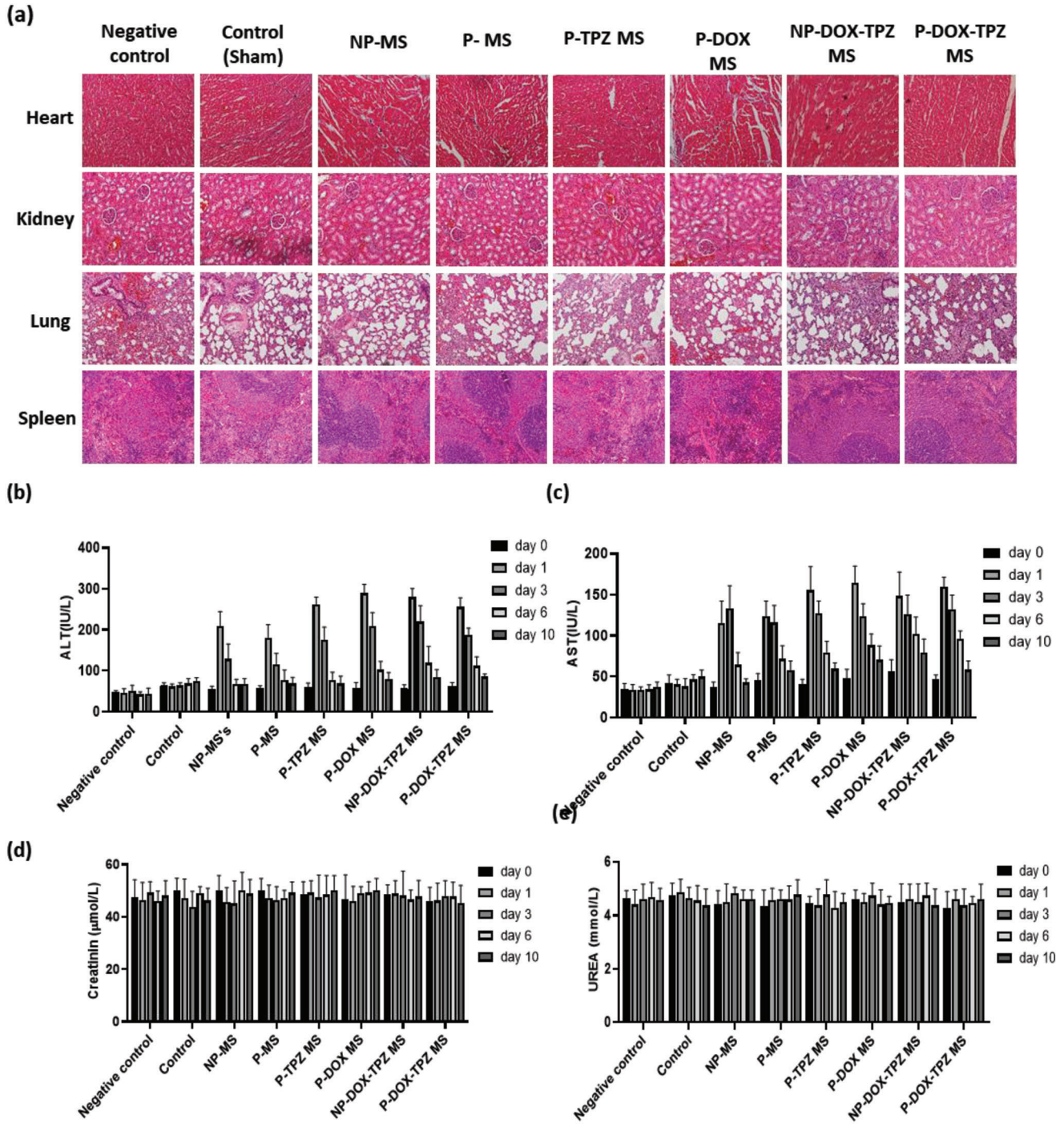

Figure 7. Histological, In-vivo toxicity analysis and blood chemical indices. a) Representative main organ tissues (heart, kidney, lung, and spleen) stained with H&E in the control group and 10 days after treatment. Plots of ALT (b), AST (c), creatinine (d), and UREA (e) levels in the serum on days 0, 1, 3, 6, and 10. Data are expressed as the mean ± SD (n = 4).

of these drugs was lower over time compared with the porous MS. The higher surface area of the porous, compared with the non-porous MS, results in a higher exposed surface area of the matrix to the flow of the released medium; thus, it might lead to a faster initial drug release rate and a more extensive drug release.[60,61] The release kinetics and MS degradation were found to be pH dependent, being notably increased at pH 6.2, compared with 7.4 in both morphologies. This can be attributed to the chemical structures, since both drugs are characterized by weak base molecules containing an amine group that can be positively charged (NH3+) at an acidic pH value, making it more soluble in released medium.[62,63] In addition, SEM images show

an enlargement of the pores on the surface of the MSs, emphasizing the acceleration of the degradation process and drug release from the PLGA matrix over time for both MS morphologies. This can related to the acidic environment that accelerates polymer hydrolysis, and thus facilitates the overall drug release and polymer degradation.[64] Over 14 days of drug release and degradation, the MS mean diameter was decreased by 10–15%. This phenomenon was comparable to the biodegradability profiles of PLGA polymeric MS depicted in other studies and found to be in line with the results in this study as well (Figure S6, Supporting Information).[65,66] The in-vivo biodegradability assay revealed loss of mass alongside size reduction and pores enlargement over a time period of 14 days. These phenomena can be attributed to the physiological degradation of the lactic and glycolic acid chains via hydrolysis reaction in rat body fluids.

Since there are no ex vivo models for embolism, one of our main tasks was to develop such a model in which we could determine the capacity of particles to occlude flow, and to measure drug perfusion, as well as the effects on cells in a physiological manner. For this purpose, we designed the EmboChip to test the embolization under in vitro conditions and under a continuous flow. When blank NP-MS were infused (without drugs), the cell viability was reduced to 65%, compared with the initial values with P-MS, which maintained 74% viability. This can be explained by the fact that the NP-MS morphology blocked the flow of the medium completely, compared with P-MS, which allowed a mild yet continuous flow, exposing the cells to fresh medium and essential nutrients throughout the experiment. However, when a drug-loaded MS was used, an opposite trend was observed. N1-S1 cells treated with the NP-DOX-TPZ MS exhibited a cell viability of 52%, compared with the 24% achieved with P-DOX-TPZ MS.

Finally, given the promising results in cell assays, the antitumor effects and biosafety profile of the drug-loaded PLGA MS were investigated in the orthotopic rat hepatoma model. Rat livers treated with blank NP-MS via hepatic artery embolization exhibited a reduced tumor volume compared with the sham group. The hepatic artery is the main source of blood for most liver tumors, suppling over 90% of the blood to the tumor, whereas normal liver parenchyma receives only 25% of its blood supply from the artery, with the remaining 75% coming from the portal vein.[67] In the sham group, the tumors continued to receive oxygen, blood, and nutrients via the hepatic artery, whereas in the treated group, these essential supplies were significantly curtailed, leading to smaller tumor volumes, as shown in other studies as well as ours.[68]

When drug-loaded MS were administered, the tumor volumes were dramatically reduced. This was most noticeable in the dual therapy group of P-DOX-TPZ MS. Surprisingly, porous MS that contained TPZ along P-TPZ-MS were equally effective as the combination when applied with non-porous particles (NP-DOX-TPZ-MS). These results may be explained by the effect of the microenvironment on the drug's activity, as shown for weak acid or base chemotherapies,[69] considering that most tumors have a pH of between 5.6 and 6.8.[70] Skarsgard et al. found that TPZ-induced DNA damage was pH dependent and was more effective at an acidic pH.[71] On the other hand, DOX HCL's inherent chemical characteristics make it positively charged in an acidic environment; thus, it may be less permeable to cells through diffusion, and hence less effective in tumor inhibition.[72] Although current clinically available TACE therapies largely use DOX as the main cytotoxic agent, this may not be an ideal choice when accounting for the harsh hypoxic conditions induced by embolization, which may reduce its effectiveness in the challenging *in-vivo* environment. Nevertheless, P-DOX-TPZ-MS showed a substantial reduction in tumor growth compared to other treated groups. This finding might be explained by combining both dual drug therapy and the particle's porous morphology.

In agreement with our in vitro results, analysis of drug distribution in tumors (Figure 5j-n) revealed that liver tumors treated with drug-loaded porous MS contained more drug compared with liver tumors treated with non-porous MS morphology. The high surface area of the porous structure, the sustained drug release, and the ease of administration of MS via the microcatheter and MS flowability, which can allow the particles to reach the inner parts of the tumor, might lead to a higher therapeutic efficacy and reduced off-target damage to the healthy liver parenchyma compared with whole MS. This signifies that the localized drug accumulation in tumor tissue was affected by MS morphology, whereas the group treated with the porous MS had a higher drug retention in tumor tissue. This fact may also explain the gap in tumor volume inhibition seen 4 days after embolization using P-DOX-TPZ-MS, emphasizing the claim that high and precise local delivery may benefit the therapeutic outcome.

The efficacy studies in the tumor rat model revealed a synergy with the dual treatment, which was also demonstrated in vitro using the optimal molar ratio (D:T 2:1, Figure 1d). This is in line with other studies showing that combinations of drugs may lead to better therapeutic responses while using lower concentrations and frequencies due to the complementary or adjuvant mechanism of action.[73,74] This efficacy was also supported by the histological analysis (Figure 6a–c). The sham group exhibited a larger tumor cell density than the other groups; this denotes a high degree of malignant lesions. In contrast, H&E staining resulted in the near-total necrosis of tumors treated by DOX-TPZ MS. Moreover, the calculated indices for Caspase-3 and Ki-67 showed the superior performance and anti-tumor proliferation of P-DOX-TPZ-MS compared with the other MS. Tumor tissues in P-DOX-TPZ-MS showed an incremental necrosis and a higher apoptosis rate in comparison with these groups, suggesting a better synergistic embolic agent by the complementary mechanism of action of both drugs discussed above. Furthermore, as CD-31 expression is closely linked to tumor angiogenesis and as an indicator of vascularization, we looked at its expression using immunohistochemical staining as a sign of tumor MVD. The analysis results revealed that P-DOX-TPZ-MS group characterized with low MVD rate and overall low tumor growth rate compared to other treated groups, implying that DOX-TPZ drug combination may reduce tumor angiogenesis (Figure S5, Supporting Information).

Finally, a fluorescence image of the tumor liver treated with NP-DOX-TPZ and P-DOX-TPZ-MS demonstrates the striking advantage of the porous MS morphology in the penetration and distribution of drugs into the tumor bed (Figure 6e,h).

Importantly, our biosafety studies indicated that the retention of drug-loaded MS in the tumor area did not lead to visible systemic effects on the tested organs (i.e., the heart, kidney, lung, and spleen). Although the values of the Creatinine (Cr) and blood urea nitrogen (Bun) remained steady, an elevation, followed by a gradual decrease in the liver enzymes ALT and AST,

indicates a transient liver injury due to TACE and the recovery of liver function, as expected.

4. Conclusion

Well-characterized porous drug delivery system for TACE treatment carrying a combination of DOX and TPZ was studied for its capacity to enhance the biological effects in liver embolism. Three liver cancer cell lines, HepG2, Huh7, and N1-S1, were found to respond differently to chemotherapy treatments under normoxia and hypoxia regimens, whereas hypoxia generally lowers the effect of DOX but can activate TPZ as hypoxia activating pro-drug. The synergistic effects of DOX and TPZ revealed that a drug combination molar ratio of D:T 2:1, in their free form, as well as embedded in PLGA MS, provides an optimal and enhanced inhibiting growth effect on N1-S1 rattus hepatoma cells. The drug-eluting beads were fabricated by microfluidics and acquired uniform parameters. The porous MSs showed high compressibility suggesting better fixation and mobilization in the capillaries post embolism. In the animal studies, P-DOX-TPZ-MS were the most effective in inhibiting the proliferation of N1-S1 hepatoma cells, exhibiting an adequate embolic effect, as well as high intra-tumoral drug concentration with low systemic exposure, as opposed to NP-DOX-TPZ-MS and other tested embolic agent groups. In addition, we observed a decrease in the expression of CD-31 and MVD in the P-DOX-TPZ-MS group, both of which are related to the treatment prognosis.

Our results indicate that the common practice of vascular blockage by combining chemotherapy might not be ideal to treat blood-rich solid tumors and that the treatment should be designed to meet the increased hypoxia in the tumor microenvironment. Finally, our results suggest that porous MSs releasing DOX and TPZ can be a promising and efficient candidate delivery system for the therapy of liver cancer using the TACE method that should potential be further tested clinically.

5. Experimental Section

Materials: Poly(D,L-lactic-co-glycolic acid) (PLGA) (Mw: 76000-115000; lactic acid:glycolic acid = 75:25), dichloromethane (DCM, Bio-Lab, Jerusalem, Israel), polyvinyl alcohol (PVA M_w 67000, Sigma–Aldrich), double distilled water (DDW), ammonium bicarbonate (ABC, NH_4HCO_3, Sigma–Aldrich), DOX hydrochloride (E.D.Q.M, Strasbourg, France), tirapazamine (TPZ, E.D.Q.M, Strasbourg, France), isopropanol (Bio-Lab, Jerusalem, Israel), Freeprint ortho resin printing polymer (Detax GmbH and Co. KG, Ettlingen, Germany), cyclosporine A (Novartis Pharma Stein AG, Bazel, Switzerland), fetal calf serum (FCS, Sigma-Aldrich), phosphate-buffered saline (PBS, Sigma–Aldrich), Tween 80 (Sigma–Aldrich), matrigel (Sigma–Aldrich), Evan's blue (Sigma–Aldrich) were used.

Cell Lines: The N1-S1 (CRL-1604; ATCC, Manassas, VA, USA), HepG2 (ATCC, Manassas, VA, USA), Huh-7 (Thermo Fisher Scientific, Waltham, MA, USA) were obtained and cultured in Iscove's Modified Dulbecco's (IMDM) Medium (Gibco, Life Technologies Limited, UK), RPMI-1640 (Life Technologies, MA, USA) and Dulbecco's Modified Eagle's (DMEM, Life Technologies, MA, USA), respectively. The media were supplemented with 10% fetal bovine serum (Life Technologies, MA, USA) and a 1% penicillin/streptomycin mixture. Cells were cultured either under normoxic conditions (21% O2, 5% CO_2) or in the inflatable hypoxia chamber (1% O2, 5% CO_2) and were placed at 37 °C in a humidified incubator. The viability of the cells was tested with Trypan blue staining, which confirmed >90% cell viability prior to the tumor induction procedure (for N1-S1).

Cell Culture—DOX Cytotoxicity Assay for Cells: Huh-7, HepG2, and N1-S1 cells were cultured in their specific medium as previously depicted. The cells were seeded into 96-well plates at a density of 1.0×10^4 cells per well and pre-incubated overnight. Thereafter, the cells were given either monotherapies of DOX (0.01–1000 µM) and hypoxia (hypoxia chamber) or a combination of DOX and hypoxia. The medium was removed from the wells and 200 µL of fresh medium containing DOX was added to each well and placed back in the incubator for 6,12, 24, or 72 h. This was followed by incubation under normoxic and hypoxic conditions for 48 h; then WST-1 reagent (Sigma-Aldrich, St. Louis, MO, USA) was added to each well for viability detection and incubated at 37 °C for 1 h. Absorbance was measured at 450 nm using a plate reader (Wallac 1420 VICTOR plate-reader, Perkin-Elmer Life Sciences, Shelton, CT, USA). n = 7 for each treatment condition.

Cell Culture—DOX and TPZ Toxicity in the N1-S1 Cell Line: N1-S1 cells were cultured in their specific medium as described above. First, the cells were seeded in 96-well plates at a density of 1.0×10^4 cells per well and pre-incubated overnight. Increasing concentrations of DOX and TPZ were prepared in a PBS (pH 7.4) solution. Next, 50 µL of free drug solution and other molar combinations (free DOX (D), free TPZ (T), D/T = 3/1, D/T = 2/1, D/T = 1/1, D/T = 1/2, D/T = 1/3) was added to each well. This was followed by incubation under normoxic and hypoxic conditions for 48 h; then WST-1 reagent was added to each well for viability detection and incubated at 37 °C for 1 h. Absorbance was measured at 450 nm using a plate reader. Similar procedures were used to test the cell viability of N1-S1 cells that had been exposed to drug-loaded and blank PLGA MS. $n = 7$ for each treatment condition.

Western Blotting: HIF-1a levels were determined in the N1-S1, HepG2, and Huh-7 cell lines under hypoxic and normoxic conditions. The cells were grown in their appropriate medium until they reached ≈80% confluency and were lysed using RIPA buffer (the radioimmunoprecipitation assay buffer). Then, the mixture was centrifuged, the cell membrane pellet was discarded, and the supernatant with proteins (50ug) was transferred electrically to SDS-polyacrylamide gel electrophoresis (100 mV, 1 h) and then to nitrocellulose membranes using a trans-blot turbo transfer system (2.5A, 25 V, 6 min, Bio-Rad, CA, USA). The membranes were blocked for 1 h with 5% bovine serum albumin (BSA, VWR chemicals, Solon, OH, USA) and then incubated for 24 h first with antibody mouse anti-human HIF-1a (Abcam, USA) overnight at 4 °C, followed by goat anti-mouse IgG for 1 h at room temperature. Next, the membranes were washed again, and 2 mL of the chemiluminescence substrate for HRP (Pierce, Thermo Scientific, MA, USA) were added for 2 min. The blots were imaged with a Bio-Rad gel imaging system and quantified with ImageJ software. β-Actin AC-15 antibody (Abcam, USA) was used as the loading control for normalization purposes. The antibody dilutions were used according to the manufacturer's instructions.

DOX-TPZ Polymeric MS Synthesis: PLGA microspheres loaded with DOX and TPZ were prepared using a microfluidic flow-focused chip design based on an adjusted solid-in-oil-in-water (S/O/W) method.[59] Briefly, PLGA 75:25 polymer was dissolved in 1 mL of DCM and gently poured into a glass vessel containing DOX TPZ at various molar ratios dissolved in 1 mL dimethyl sulfoxide (DMSO). For solvent evaporation, the glass vial was held by tongs, and its bottom was dipped inside a warm water (50 °C) bath, and a gentle nitrogen gas stream was applied from above for 5 h. Next, the DOX-TPZ-polymer film was dissolved in 4 mL DCM and homogenized (an MICCRA homogenizer disperser D-9, Heitersheim, Germany) with 1.5 mL of 1% (*w/v*) of ABC solution for 3 min at 6000 rpm for fabrication of porous MS). Then, the homogenized solution was gently perfused into the microfluidic droplet generation chip using a glass syringe. The flow-focused chip design consisted of a cross junction, in which the primary homogenized emulsion entered through a central channel and was squeezed at the orifice by two parallel streams of 1% (w/v) PVA solution to form a controlled droplet breakup. The fabricated MS were stirred in the chemical hood with an overhead propeller at 400 rpm overnight to ensure complete organic solvent evaporation. The porosity was achieved by a gas-foaming technique using ammonium bicarbonate as a gas-foaming

agent at the primary emulsion formation (O/W). Once the double emulsion form, small micro gas-bubbles (carbon dioxide and ammonia gas bubbles) spontaneously appear during the solvent evaporation process. The MS were washed 3 times with DDW and centrifuged at 8000 rpm for 3 min. Finally, to prepare solidified particles, the MS pellet was resuspended with DDW and frozen overnight at −80 °C and lyophilized (Freezone 6 plus, Labconco, Kansas City, MO, USA) to produce a dry powder of MS for further storage (−20 °C) and characterization. Control polymeric MS (blank, without drugs) were prepared similarly.

Particle Morphology and Size Characterization: The morphology of fabricated MSs was characterized and imaged using a fluorescent microscope (Nikon Eclipse Ti2 Inverted Research Microscope, NY, USA) as well as a Scanning Electron Microscope (SEM, FEI Quanta 200 microscope, Waltham, MA, USA). A small amount of the samples was spread on a conductive adhesive carbon tape attached to a SEM grid and a thin film of Pd/Au coating was sputtered onto the sample (SC7620 Spatter coater, Laughton, East Sussex, UK). The mean MS diameter was measured using Mastersizer 3000 (Malvern, Cambridge, UK). The elastic compressibility was tested using a microfluidic chip consisting of a converged tunnel of 400 to 50 µm. The PDMS chip dimensions and the interior compartment are depicted in Figure S4 (Supporting Information).

3D Printing Process: For the 3D printing of the microfluidic device, we used a digital light processing—stereolithography printer (Asiga Max-X27 UV, Sydney, Australia). This 3D printer had a LED light source with a 385 nm UV wavelength. The XY pixel resolution of the printer's projectors was 27 µm and its minimum Z plane resolution was 1 µm. The maximum build size, X, Y, and Z was 51.8 mm × 29.2 mm × 75 mm, respectively. All the objects were designed with Autodesk AutoCad software (Q.70.0.0 AutoCAD 2020, San Rafael, CA, USA) and sent to be printed as an STL file. The printing process was carried out as follows: The build plate was lowered into the vat to a predetermined height and the DLP projected the first slice of the design for a predetermined amount of time. The build plate was raised for a few seconds and lowered again into the vat to allow proper printing of layers. Once finished, the printed object was gently removed from the build plate, rinsed with isopropyl alcohol in a sonicator bath (Bandelin) for 3 min, dried using air pressure, and finally cured in a UV oven for 5 min (PCU Led, Dreve).

Development of EmboChip, an In Vitro Microfluidic Model for Embolism—Embolization and Microfluidic Chip Fabrication: A specially designed microfluidic chip (EmboChip) mimicking the microvascular construct was prototyped in polydimethylsiloxane (PDMS) using a 3D printing technology and soft lithography. The chip was designed using CAD software (AutoCAD 2020); it consisted of a main chamber, two inputs, and two outputs (Figure 4a+b). After the printing process ended, a mixture of PDMS (Sylgard 184, Dow Corning) and a curing agent (Sylgard 184, Dow Corning) was prepared using a ratio of 10:1, respectively. The PDMS was poured into the mold framework and put into a vacuum desiccator for 1 h to remove all air bubbles inside. Next, the mold was placed in an oven (Memmert) set at 65 °C overnight. To create the microfluidic device, the cured PDMS was gently peeled from the mold, punched to create the inlets and outlets, and treated with oxygen plasma at high power (Diener electronic) before being attached to a plasma-treated clean glass slide. Finally, the microfluidic chip was placed on a hot plate set at 50 °C for 10 min to ensure good bonding of the PDMS to the glass slide. The PDMS chip dimensions and the interior compartment are depicted in Figure 4a.

Development of EmboChip, an In Vitro Microfluidic Model for Embolism—In Vitro Embolization Experiment: The EmboChip was connected to a microfluidic electric pump and a pre-seeding cell wash process was carried out as follows: 70% ethanol, PBS, poly-L-lysine, and PBS—10 min each at a flow rate of 40 µL min^{-1}. After the wash was completed, the left-side inlet and the right-side outlet were closed and a gentle flow of N1-S1 cells (20×10^5) started to flow from the upper inlet to the main chamber and seed. After the cells filled the chamber, the upper and bottom inlets closed; then the left-side inlet was opened and connected to a syringe full of IMDM media allowing flow (10 µL min^{-1}) of fresh media to the cells. After a 24 h post-seeding, the embolization procedure was carried out; porous and non-porous drug-loaded MS were introduced into the microfluidic device at an appropriate flow rate (10 µL min^{-1}) and time-lapse images were taken. Blank MS was used as the control. Each experiment was conducted in triplicate.

Production of a Microfluidic Dissolution Chip Using 3D Printing: A transparent bottom 3D-printed microfluidic chip, which was reported in our previous study, was used to evaluate the degradation and the drug release rate from the embolic MS.[59] Briefly, a glass slide was pre-activated in 2% of 3-(Trimethoxysilyl)-propyl methacrylate (TMSPMA), followed by submersion in 100% ethanol. Afterward, the glass was placed in an oven (set for 105 °C) and allowed to cool prior to the printing process. Prior to initiating the 3D printing process, and for using the glass slide as the chip substrate, it was first attached to the printer's platform with a few drops of resin polymer. At the end of the printing process, the glass with the printed resin was gently detached, cleaned, and cured as described above.

In Vitro Drug Release, Degradability, and Biodegradability Assay: An MS release study was conducted using a microfluidic dissolution chip at two different pH values (pH 7.4 and pH 6.2). DOX-TPZ polymeric MS were gently injected into a "V" shaped trap microfluidic dissolution chip. The chip was then connected to a 60 mL syringe filled with PBS release medium containing 0.1% (w/v) tween 80 and connected to a microfluidic dual syringe pump (Chemyx Fusion100 Stafford, TX, USA). The system was maintained at 37 °C for 14 days and samples were collected at predetermined times. Samples of 500 µL were collected from the test vessel solution and immediately measured by a UV–vis spectrophotometer at 480 nm (DOX) and at 271 nm (TPZ) wavelengths using a UV–vis spectrophotometer. Immediately after the measurement, the sample was returned to the test vessel. The percentage of release was calculated by normalizing the obtained data at each time point with the cumulative total amount, based on a calibration curve of the drugs.

The degradation rate of the drug-loaded MS was investigated using the microfluidic dissolution chip as well as the transparent bottom glass slide on which the chip was printed. Next, 10 mg of MS was loaded into the chip and filled with a mixture of 50% (v/v) FCS with PBS, simulating main blood components, and placed at 37 °C for 14 days. To monitor and estimate the degradation, SEM images were taken on days 0, 7, and 14. In addition, an in vivo evaluation of biodegradability of the porous MS conducted via rat liver embolization procedure and tested in three different time periods, day 0, 7, and 14. Data can be seen in Figure S6 (Supporting Information). Blank MS was used as the control. Each experiment was conducted in triplicate.

Drug Content and Encapsulation Efficiency: Drug content (DC) and encapsulation efficiency (EE) of both DOX and TPZ were determined by dissolving 5 mg of the fabricated MS (dried powder) in 0.5 mL of DMSO, followed by filtration and dilution to be detectable within a standard calibration curve range (0.5–20 mg mL^{-1}). A UV–vis spectrophotometer (BiochromTMUltrospec 2100 Pro) was used to determine the absorbance of encapsulated DOX and TPZ in the prepared formulations with an absorbance wavelength of 480 and 241, respectively. The percentage of EE and the DC of the MS was calculated as follows:

$$\text{Encapsulation efficiency (EE\%)} = \frac{\text{Mass of Dox/TPZ in MS}}{\text{Initial amount of Dox/TPZ}} \quad (1)$$

$$\text{Drug content (DC\%)} = \frac{\text{Mass of DOX/TPZ in MS}}{\text{Mass of MS}} \quad (2)$$

An Orthotopic Rat Model for HCC: Twenty-four male Sprague–Dawley (SD) rats, initially weighing ≈480–500 g, were used for this study. Isoflurane gas was used to anesthetize each rat prior to tumor implementation and the embolization procedures. For tumor induction, the rat abdomen was shaved, and HF-US was performed using a Vevo 3100 HF-US system (Fujifilm VisualSonics, Inc., Ontario, Canada) with a 250 MHz transducer that was held above the animal in supine position. Next, the N1-S1 (1.5×10^6 cells prepared in 50 µL of sterile PBS and 50 µL of matrigel) cell line was slowly injected into the liver parenchyma using a 23G needle. A mild pressure was applied on the injection site for 2 min to avoid the reflux of injected cells. To prevent the spontaneous tumor regression of the N1-S1 hepatoma, cyclosporine A (20 mg kg^{-1} d^{-1}) was administered

subcutaneously from 1 day prior to the tumor implementation, and until 3 days after the intrahepatic injection. Tumor growth was monitored by an HF-US machine. The rats were maintained under high health status conditions and specifically had a pathogen-free status. All institutional and national guidelines for the care and use of laboratory animals were followed, and protocols were approved by The Hebrew University of Jerusalem Ein Kearem Medical School Institutional Animal Care and Use Committee (approval no. MD–19–15810–5).

Hepatic Artery Embolization: The orthotopic liver cancer rat model was used to assess TACE therapy. Two weeks post-cancer cell implementation, when tumors reached >1 cm, the rats were assigned to the control, hepatic artery chemoembolization, or sham treatment groups. Administration of MS via microcatheter was conducted by a senior experienced interventional radiologist. Following anesthesia with isoflurane gas, the rat was placed in supine position, the left neck side was gently dissected, and the left common carotid artery (LCCA) was carefully isolated from the vagus nerve. Then, the LCCA was cannulated by a 24-gauge intravenous venflon (Angiocath; BD Biosciences, San Jose, CA, USA), a 1.3-Fr. Headway Duo microcatheter (MicroVention, Tustin, California, USA) was modified to 50 cm in length and carefully inserted over an 0.01-inch guidewire (Transcend; Boston Scientific, Marlborough, MA, USA), after removal of the venflon. The catheter/guidewire combination was then used to cannulate the proper hepatic artery with continuous X-ray fluoroscopic guidance (OEC 9900 Elite, GE Healthcare, USA). Once placed in its position, 100 µl of nitroglycerine (0.1 mg kg^{-1}) was slowly injected to reduce vasospasms; the embolization was performed with 40–50 µm microspheres with an adjusted dose of 1 mg kg^{-1}. The sham procedure was performed by inserting the catheter similarly, injecting saline without embolization. After embolization, the microcatheter was removed, the left common carotid artery was ligated, the neck incision was closed, and the rats were allowed to recover.

In Vivo Tissue Distribution of DOX and TPZ: The DOX and TPZ concentrations in normal liver parenchyma and the liver tumor regions were measured. The differently treated group livers were dissected on day 10 after embolization. To determine the drug concentrations in the specimens, each tissue was homogenized with DW (1:5 w/w) and analyzed for the final drug concentrations using high-performance liquid chromatography (HPLC, SHIMADZU, OR, USA). Briefly, DOX was quantitatively determined by HPLC using a C18 column (Gemini 5 µm NX-C18 110 Å, LC Column 250×4.6 mm, CA, USA). The mobile phase consisted of 10 mM potassium phosphate buffer (pH 2.5, adjusted with HCl) and acetonitrile dissolved with a 0.1% triethylamine mixture (73:27). The injection volume was 20 µL, the flow rate was set to 1 mL min^{-1}, and the detection wavelength was 254 nm. The mobile phase for TPZ determination consisted of a mixture of acetonitrile and DW (13:87). The injection volume was 20 µL, the flow rate was set to 1.5 mL min^{-1}, and the detection wavelength was 460 nm. The lower detection limit was 15 ng mL^{-1} for both drugs.

Biosafety, Histopathological, and Immunohistochemical Analysis: The biosafety of the MS was evaluated by both histological staining of the peripheral organs (heart, kidney, lung, and spleen) and analysis of the central blood biochemistry analytes (ALT, AST, UBN, and Cr) that were obtained from rat serum during the treatment follow-ups. On day 10 post-embolization treatments, all rats were euthanized. Livers were collected and washed in cold PBS, cut into small axial pieces, and fixed by immersion in 4% (*w/v*) paraformaldehyde. Afterward, the tissues were blocked in paraffin, cut, and stained with Hematoxylin and Eosin (H&E) for basic analysis and histological examination. Furthermore, to evaluate the degree of apoptosis and tumor proliferation, Caspase-3 (Abcam, USA), Ki-67 (Abcam, USA), and CD-31 (Abcam, USA) staining was performed according to the manufacturer's instructions, respectively. Microvessel density (MVD) was performed as previously reported.[75] The quantitative assessment was performed on low (X40) and high (X100) magnification and average counts were recorded. Not less than three fields were examined. Images were obtained using an Eclipse Ti2 inverted microscope (Nikon, Tokyo, Japan). Analysis and counting of positive staining cells were conducted using NIS-Elements Microscope Imaging Software.

Statistical Analyses: Statistical analysis of the data was done using a two-tailed *t*-test and analysis of variance (ANOVA), followed by applying the Tukey test. All experiments were repeated at least three times, and the data were shown as the mean ± SD. The type of tests and analysis performed in each experiment and the statistical significance are depicted in the figure legends. All statistical analyses were performed using GraphPad Prism 8 (GraphPad Software, Inc., CA, USA). A p-value < 0.05 was considered statistically significant.

Supporting Information

Supporting Information is available from the Wiley Online Library or from the author.

Acknowledgements

The authors would like to thank Prof. R. Abramovitch and N. Abudi from the Wohl Institute for Translational Medicine and D. Kushnir from the Center for Innovative Surgery for their guidance and technical support. This project received funding from The Israeli Innovation Authority (Kamin fund, no. 3011005092), The European Research Council (ERC-StG, grant agreement no. 0305260), and ERC-POC under the European Union's Horizon 2020 research and innovation program.

Conflict of Interest

The authors declare no conflict of interest.

Data Availability Statement

The data that support the findings of this study are available from the corresponding author upon reasonable request.

Keywords

embolization, hepatocellular carcinoma, hypoxia, poly(lactic-*co*-glycolic acid), trans-arterial chemoembolization

Received: May 12, 2023
Published online: June 26, 2023

[1] B. Muz, P. de la Puente, F. Azab, A. K. Azab, *Hypoxia* **2015**, 83.
[2] M. C. Bosco, G. D'Orazi, D. Del Bufalo, *J Exp Clin Cancer Res* **2020**, *39*, 1.
[3] D. Chakraborty, E. Sarkar, *Cancers* **2022**, *14*, 2798.
[4] N. E. Rich, A. C. Yopp, A. G. Singal, *J Oncol Pract* **2017**, *13*, 356.
[5] R. Laube, A. H. Sabih, S. I. Strasser, L. Lim, M. Cigolini, K. Liu, *J Gastroenterol Hepatol* **2021**, *36*, 618.
[6] H. C. Kim, K. T. Suk, D. J. Kim, J. H. Yoon, Y. S. Kim, G. H. Baik, J. B. Kim, C. H. Kim, H. Sung, J. Y. Choi, K. H. Han, S. H. Park, *World J. Gastroenterol.* **2014**, *20*, 745.
[7] R. A. Sheth, S. Sabir, S. Krishnamurthy, R. K. Avery, Y. S. Zhang, A. Khademhosseini, R. Oklu, *J Funct Biomater* **2017**, *8*, 12.
[8] B. Liang, C. S. Zheng, G. S. Feng, H. P. Wu, Y. Wang, H. Zhao, J. Qian, H. M. Liang, *Cardiovasc Intervent Radiol* **2010**, *33*, 806.
[9] E. Ueshima, H. Nishiofuku, H. Takaki, Y. Hirata, H. Kodama, T. Tanaka, K. Kichikawa, K. Yamakado, T. Okada, K. Sofue, M. Yamaguchi, K. Sugimoto, T. Murakami, *Liver Cancer* **2020**, *9*, 63.
[10] T. K. Rhee, J. Y. Young, A. C. Larson, G. K. Haines, K. T. Sato, R. Salem, M. F. Mulcahy, L. M. Kulik, T. Paunesku, G. E. Woloschak, R. A. Omary, *J Vasc Interv Radiol* **2007**, *18*, 639.

[11] Y. Su, B. Zhang, R. Sun, W. Liu, Q. Zhu, X. Zhang, R. Wang, C. Chen, *Drug Deliv* **2021**, *28*, 1397.
[12] J. W. Choi, J. H. Park, H. R. Cho, J. W. Chung, D. D. Kim, H. C. Kim, H. J. Cho, *Sci. Rep.* **2017**, *7*, 554.
[13] Y. J. Liang, H. Yu, G. Feng, L. Zhuang, W. Xi, M. Ma, J. Chen, N. Gu, Y. Zhang, *ACS Appl. Mater. Interfaces* **2017**, *9*, 43478.
[14] X. Zhu, M. Duan, L. Zhang, J. Zhao, S. Yang, R. Shen, S. Chen, L. Fan, J. Liu, *Adv. Funct. Mater.* **2023**, *2209413*, 554.
[15] W. Chen, A. Palazzo, W. E. Hennink, R. J. Kok, *Mol. Pharmaceutics* **2017**, *14*, 459.
[16] D. Klose, F. Siepmann, K. Elkharraz, S. Krenzlin, J. Siepmann, *Int. J. Pharm.* **2006**, *314*, 198.
[17] Z. Zhang, X. Wang, B. Li, Y. Hou, J. Yang, L. Yi, *Drug Deliv* **2018**, *25*, 166.
[18] C. Cai, S. Mao, O. Germershaus, A. Schaper, E. Rytting, D. Chen, T. Kissel, *J Microencapsul* **2009**, *26*, 334.
[19] O. Tacar, P. Sriamornsak, C. R. Dass, **2013**, 157.
[20] J. Cox, S. Weinman, *Hepatic Oncol.* **2016**, *3*, 57.
[21] J. W. Wojtkowiak, D. Verduzco, K. J. Schramm, R. J. Gillies, *Mol. Pharmaceutics* **2011**, *8*, 2032.
[22] B. Wang, X. C. Yu, S. F. Xu, M. Xu, *J Nanobiotechnology* **2015**, *13*, 22.
[23] Y. Mi, J. Zhao, S. S. Feng, *J. Controlled Release* **2013**, *169*, 185.
[24] Y. Li, L. Zhao, X. F. Li, *Front Oncol* **2021**, *11*, 1.
[25] W. H. Lin, S. H. Yeh, K. H. Yeh, K. W. Chen, Y. W. Cheng, T. H. Su, P. Jao, L. C. Ni, P. J. Chen, D. S. Chen, *Proc. Natl. Acad. Sci. USA* **2016**, *113*, 11937.
[26] P. Ma, J. Chen, H. Qu, Y. Li, X. Li, X. Tang, Z. Song, H. Xin, J. Zhang, J. Nai, Z. Li, Z. Wang, *Drug Deliv* **2020**, *27*, 1412.
[27] T.-C. N. M. Chou, https://www.combosyn.com, **2006**. Access date 1 November 2022.
[28] T. C. Chou, *Synergy* **2018**, *7*, 49.
[29] R. Y. Huang, L. Pei, Q. Liu, S. Chen, H. Dou, G. Shu, Z. X. Yuan, J. Lin, G. Peng, W. Zhang, H. Fu, *Front Pharmacol* **2019**, *10*, 1.
[30] B. Amoyav, O. Benny, *Appl. Nanosci.* **2018**, *0*, 0.
[31] B. Amoyav, O. Benny, *Polymers.* **2019**, *11*, 419.
[32] B. Vollmar, M. D. Menger, *Physiol. Rev.* **2009**, *89*, 1269.
[33] M. Q. Zhang, D. N. Sun, Y. Y. Xie, G. Y. Peng, J. Xia, H. Y. Long, B. Xiao, *Br. J. Radiol.* **2014**, *87*, 20130670.
[34] F. Capone, E. Guerriero, A. Sorice, G. Colonna, G. Storti, J. Pagliuca, G. Castello, S. Costantini, *Sci. World J.* **2014**, *2014*, 1.
[35] L. Solorio, H. Wu, C. Hernandez, M. Gangolli, A. A. Exner, *Ther Deliv* **2016**, *7*, 201.
[36] A. Y. Chang, M. Wang, *Anticancer Drugs* **2013**, *24*, 251.
[37] T. Lee, T. Lau, I. Ng, *Cancer Chemother. Pharmacol.* **2002**, *49*, 78.
[38] D. M. Evans, J. Fang, T. Silvers, R. Delosh, J. Laudeman, C. Ogle, R. Reinhart, M. Selby, L. Bowles, J. Connelly, E. Harris, J. Krushkal, L. Rubinstein, J. H. Doroshow, B. A. Teicher, *Cancer Chemother. Pharmacol.* **2019**, *84*, 359.
[39] F. Kullenberg, O. Degerstedt, C. Calitz, N. Pavlović, D. Balgoma, J. Gråsjö, E. Sjögren, M. Hedeland, F. Heindryckx, H. Lennernäs, *Cells* **2021**, *1717*, https://doi.org/10.3390/cells10071717.
[40] G. N. Masoud, W. Li, *Acta Pharm. Sin. B* **2015**, *5*, 378.
[41] C. Bowyer, A. L. Lewis, A. W. Lloyd, G. J. Phillips, W. M. MacFarlane, *Anticancer Drugs* **2017**, *28*, 771.
[42] R. Shi, C. Liao, Q. Zhang, *Cells* **2021**, *10*, 678.
[43] M. Fei, J. Guan, T. Xue, L. Qin, C. Tang, G. Cui, Y. Wang, H. Gong, W. Feng, *Cell. Mol. Biol. Lett.* **2018**, *23*, 46.
[44] Donahoe, *Mol. Cell. Biochem.* **2012**, *23*, 612.
[45] R. Gui, R. Huang, J. H. Zhang, X. H. Wen, X. M. Nie, *Oncol Rep* **2016**, *35*, 2216.
[46] E. Christidi, L. R. Brunham, *Cell Death Dis.* **2021**, *12*, 339.
[47] A. Meredith, C. R. Dass, **2016**, *68*, 729.
[48] G. Ajnai, C. Cheng, T. Kan, J. Lu, S. Rahayu, A. Chiu, J. Chang, **2022**.
[49] T. Moriwaki, S. Okamoto, H. Sasanuma, H. Nagasawa, S. Takeda, S. Masunaga, K. Tano, *Chem. Res. Toxicol.* **2017**, *30*, 699.
[50] S. B. Reddy, S. K. Williamson, *Expert Opin Investig Drugs* **2009**, *18*, 77.
[51] D. Guo, S. Xu, W. Yasen, C. Zhang, J. Shen, Y. Huang, D. Chen, X. Zhu, *Biomater. Sci.* **2020**, *8*, 694.
[52] S. Streck, H. Neumann, H. M. Nielsen, T. Rades, A. McDowell, *Int J Pharm X* **2019**, *1*, 100030.
[53] K. Agrawal, *xPharm Compr. Pharmacol. Ref.* **2007**, 1.
[54] T. Q. Wang, Z. G. Yang, *J. Sound Vib.* **2004**, *273*, 969.
[55] Z. Pan, J. Ding, *Interface Focus.* **2012**, *2*, 366.
[56] K. Hidaka, M. Nakamura, K. Osuga, H. Miyazaki, S. Wada, *J. Mech. Behav. Biomed. Mater.* **2010**, *3*, 497.
[57] Y. Wang, X. Qiao, X. Yang, M. Yuan, S. Xian, L. Zhang, D. Yang, S. Liu, F. Dai, Z. Tan, Y. Cheng, *Cancer Biol. Med.* **2020**, *17*, 237.
[58] K. Thananukul, C. Kaewsaneha, P. Opaprakasit, N. Lebaz, A. Errachid, A. Elaissari, *Adv. Drug Delivery Rev.* **2021**, *174*, 425.
[59] B. Amoyav, Y. Goldstein, E. Steinberg, O. Benny, *Pharmaceutics* **2021**, *13*, 1.
[60] S. Nishimura, T. Takami, Y. Murakami, *Colloids Surf., B* **2017**, *159*, 318.
[61] P. O. Chhattikara, **2013**, 1.
[62] S. S. Shinde, A. Maroz, M. P. Hay, A. V. Patterson, W. A. Denny, R. F. Anderson, **2010**, 2591.
[63] Y. Wang, Z. Xu, **2016**, 314.
[64] E. M. Elmowafy, M. Tiboni, M. E. Soliman, *J Pharm Investig* **2019**, *49*, 347.
[65] B. S. Zolnik, D. J. Burgess, *J. Controlled Release* **2007**, *122*, 338.
[66] H. K. Makadia, S. J. Siegel, *Polymers* **2011**, *31*, 1377.
[67] C. Charnsangavej, S. Wallace, C. H. Carrasco, W. Bechtel, *Liver Cancer* **1985**, 157.
[68] J. Folkman, *Sci. Am.* **1996**, *275*, 150.
[69] L. E. Gerweck, S. Vijayappa, S. Kozin, *Mol. Cancer Ther.* **2006**, *5*, 1275.
[70] E. Boedtkjer, S. F. Pedersen, *Annu. Rev. Physiol.* **2020**, *82*, 103.
[71] Skarsgard, **1994**, *29*, 363.
[72] A. Trebinska-Stryjewska, O. Swiech, L. J. Opuchlik, E. A. Grzybowska, R. Bilewicz, *ACS Omega* **2020**, *5*, 7979.
[73] H. Wu, H. Jin, C. Wang, Z. Zhang, H. Ruan, L. Sun, C. Yang, Y. Li, W. Qin, C. Wang, *ACS Appl. Mater. Interfaces* **2017**, *9*, 9426.
[74] I. Kim, H. J. Byeon, T. H. Kim, E. S. Lee, K. T. Oh, B. S. Shin, K. C. Lee, Y. S. Youn, *Biomaterials* **2013**, *34*, 6444.
[75] S. Bosari, A. K. C. Lee, R. A. DeLellis, B. D. Wiley, G. J. Heatley, M. L. Silverman, *Hum Pathol* **1992**, *23*, 755.